

1 **Coordination between metabolic transitions and gene expression by**  
2 **NAD<sup>+</sup> availability during adipogenic differentiation in human cells.**

3

4 Edgar Sanchez-Ramírez<sup>1+</sup>, Thi Phuong Lien Ung <sup>2+</sup>, Ximena del Toro-Rios<sup>1</sup>, Guadalupe  
5 R. Fajardo-Orduña<sup>1</sup>, Lilia G. Noriega<sup>3</sup>, Armando R. Tovar<sup>3</sup>, Juan José Montesinos<sup>4</sup>,  
6 Ricardo Orozco-Solís<sup>5</sup>, Chiara Stringari<sup>2##</sup> and Lorena Aguilar-Arnal<sup>1##</sup>

7

8 1 Departamento de Biología Celular y Fisiología, Instituto de Investigaciones  
9 Biomédicas, Universidad Nacional Autónoma de México, 04510 Mexico City, Mexico

10 2 Laboratory for Optics and Biosciences, Ecole polytechnique, CNRS, INSERM, Institut  
11 Polytechnique de Paris, 91128 Palaiseau cedex, France.

12 3. Departamento de Fisiología de la Nutrición, Instituto Nacional de Ciencias Médicas y  
13 Nutrición Salvador Zubirán, 14080 Mexico City, Mexico

14 4 Mesenchymal Stem Cells Laboratory, Oncology Research Unit, Oncology Hospital,  
15 National Medical Center (IMSS), 06720 Mexico City, Mexico;

16 5 Laboratorio de Cronobiología y Metabolismo, Instituto Nacional de Medicina  
17 Genómica, 14610 Mexico City, Mexico

18 + # These authors contributed equally to the work.

19 \*To whom correspondence should be addressed: [chiara.stringari@polytechnique.edu](mailto:chiara.stringari@polytechnique.edu)  
20 [loreaquilararnal@iibiomedicas.unam.mx](mailto:loreaquilararnal@iibiomedicas.unam.mx)

21 **ABSTRACT**

22 Adipocytes are the main cell type in adipose tissue, a critical regulator of metabolism,  
23 highly specialized in storing energy as fat. Adipocytes differentiate from multipotent  
24 mesenchymal stromal cells through adipogenesis, a tightly controlled differentiation  
25 process involving closely interplay between metabolic transitions and sequential  
26 programs of gene expression. However, the specific gears driving this interplay remain  
27 largely obscure. Additionally, the metabolite nicotinamide adenine dinucleotide (NAD<sup>+</sup>)  
28 is becoming increasingly recognized as a regulator of lipid metabolism, being postulated  
29 as promising therapeutic target for dyslipidemia and obesity. Here, we explored the  
30 effect of manipulating NAD<sup>+</sup> bioavailability during adipogenic differentiation from human  
31 mesenchymal stem cells. We found a previously unappreciated strong repressive role  
32 for NAD<sup>+</sup> on adipocyte commitment, while a functional NAD<sup>+</sup>-dependent deacetylase  
33 SIRT1 appeared crucial for terminal differentiation of pre-adipocytes. Remarkably,  
34 repressing the NAD<sup>+</sup> biosynthetic salvage pathway during adipogenesis promoted the  
35 adipogenic transcriptional program, suggesting that SIRT1 activity during adipogenesis  
36 is independent from the NAD<sup>+</sup> salvage pathway, while two photon microscopy and  
37 extracellular flux analyses suggest that its activation relies on the metabolic switch.  
38 Interestingly, SIRT1-directed control of subcellular compartmentalization of redox  
39 metabolism during adipogenesis was evidenced by two-photon fluorescence lifetime  
40 microscopy.

41

42

## 43 **Significance Statement**

44 Adipocyte differentiation occurs from mesenchymal stem cells through the adipogenic  
45 process, involving sequential activation of both transcriptional and metabolic programs  
46 in a tightly coordinated manner. However, how transcriptional and metabolic transitions  
47 reciprocally interact during adipogenic differentiation remains largely obscure. Here we  
48 describe that the metabolite NAD<sup>+</sup> suppresses adipogenesis through rewiring  
49 transcription, while a functional NAD<sup>+</sup>-dependent deacetylase SIRT1 is essential for  
50 terminal differentiation of pre-adipocytes. Using two-photon fluorescence lifetime  
51 microscopy, we created a metabolic map of NADH and lipid content simultaneously in  
52 live cells and described a new role for SIRT1 in the control of compartmentalization of  
53 redox metabolism during adipogenesis. These findings advance our understanding to  
54 improve therapeutic approaches targeting the NAD<sup>+</sup>-SIRT1 axis as treatment for  
55 obesity and dyslipemia.

56

## 57 **INTRODUCTION**

58 Adipose tissue is a crucial regulator of body metabolism through storing calories as  
59 lipids in response to excessive nutritional intake and serving as a source of energy by  
60 mobilizing these lipids during starvation, amongst others. Notably, the adipose tissue is  
61 a relevant endocrine organ, producing several adipokines such as leptin or  
62 adiponectin(1). It is primarily composed of adipocytes, and a fraction of a  
63 heterogeneous collection of cell types which include mesenchymal stem cells (MSC),  
64 endothelial precursors, immune cells, smooth muscle cells, pericytes and

65 preadipocytes(2). Disfunction of the adipose compartment is common to metabolic  
66 diseases including obesity or type 2 diabetes. Indeed, increased white adipose tissue  
67 (WAT) mass observed in obesity is due to both adipocyte hypertrophy and increased  
68 proliferation and differentiation of adipocyte progenitors(3, 4), which originate from  
69 MSCs though the adipogenic process (5, 6). Hence, understanding the mechanisms  
70 underlying adipogenesis in humans is crucial to design therapeutic strategies for  
71 prevalent metabolic dysfunctions.

72 MSCs are multipotent progenitor cells able to differentiate to osteoblasts, myocytes,  
73 chondrocytes, and adipocytes. Fate decision is determined by specific signaling  
74 pathways such as transforming growth factor-beta (TGF $\beta$ )/bone morphogenic protein  
75 (BMP) signaling, wingless-type MMTV integration site (Wnt) signaling or fibroblast  
76 growth factors (FGFs)(7, 8). In particular, the adipogenic process occurs in two major  
77 phases: commitment to progenitors and terminal differentiation; both of which are tightly  
78 regulated by intertwined transcriptional, epigenomic and metabolic transitions(8). At the  
79 transcriptional level, the master regulators of adipogenesis are the key transcription  
80 factors peroxisome proliferator-activated receptor  $\gamma$  (PPAR $\gamma$ ) and CCAAT/enhancer  
81 binding protein  $\alpha$  (C/EBP $\alpha$ )(9, 10), which promote growth arrest and the progressive  
82 expression of a lipogenic transcriptional program including the hormones adiponectin  
83 and leptin, and the lipases adipose triglyceride lipase (ATGL) and lipoprotein lipase  
84 (LPL)(8). Concomitantly, a switch from highly glycolytic to oxidative metabolism with  
85 increased mitochondrial reactive oxygen species (ROS) is essential for adipocyte  
86 differentiation(11, 12). However, how transcriptional and metabolic transitions  
87 reciprocally interact during adipogenic differentiation remains an open question.

88 During the past few years, energy metabolism is becoming increasingly recognized as  
89 an effective therapeutic target for obesity. Specifically, therapies aiming to increase  
90 endogenous nicotinamide adenine dinucleotide (NAD<sup>+</sup>) levels have been proven  
91 effective to reduce adiposity in both mouse and human(13-16). Indeed, NAD<sup>+</sup> levels  
92 decline in metabolic tissues of obese mice and humans(14, 15, 17-20), which may  
93 contribute to metabolic dysfunction by, for example, reducing the activity of SIRT1, a  
94 deacetylase using NAD<sup>+</sup> as cofactor and known to regulate mitochondrial function and  
95 metabolism(21, 22). These evidences suggest that NAD<sup>+</sup> metabolism might be a central  
96 player on adipose tissue homeostasis probably by regulating mitochondrial function and  
97 consequently, adipocyte differentiation. Along these lines, in mouse preadipocytes,  
98 NAD<sup>+</sup> synthesis through the salvage pathway and SIRT1 activity appear essential for  
99 adipogenesis(23); however, the interplay between NAD<sup>+</sup> bioavailability and SIRT1  
100 function during adipogenesis in humans remains poorly understood.

101 In this study, we explored the coordinated dynamics of the transcriptional and energy  
102 metabolism reprogramming during adipogenic differentiation of human MSC (hMSC).  
103 Using two-photon fluorescence lifetime microscopy (2P-FLIM) on live hMSC, we created  
104 a non-invasive metabolic map of NADH compartmentalization at a submicron resolution  
105 to define the dynamics of redox metabolism during adipogenesis, which appeared  
106 tightly synchronized with mitochondrial function and transcriptional reprogramming.  
107 Moreover, we described a previously unappreciated robust inhibitory role for NAD<sup>+</sup> on  
108 adipocyte commitment, while SIRT1 activity appeared essential for terminal  
109 differentiation. Surprisingly, suppressing the NAD<sup>+</sup> salvage pathway during  
110 adipogenesis led to increased expression of adipocyte markers, indicating that SIRT1

111 activation during adipogenesis doesn't depend on NAD<sup>+</sup> biosynthesis through the  
112 salvage pathway. Remarkably, SIRT1-directed control of compartmentalization of redox  
113 metabolism during adipogenesis was evidenced by 2P-FLIM.

114

## 115 **RESULTS**

### 116 **NAD<sup>+</sup> obstructs adipogenic differentiation and lipid accumulation in hMSC.**

117 To approach the question whether variations in NAD<sup>+</sup> bioavailability impact  
118 adipogenesis, we induced adipogenic differentiation in hMSCs in the presence or  
119 absence of NAD<sup>+</sup> (Figure 1A). Interestingly, NAD<sup>+</sup> treatment obstructed neutral lipid  
120 accumulation, as visualized by significantly less accumulation of Oil-red-O (ORO) stain  
121 at terminal differentiation than in non-treated (NT) cells (Figure 1A, day 16,  $P<0,01$ ,  
122 Two-way ANOVA with Tukey's post-test). Concomitantly, a treatment with FK866, a  
123 potent and highly selective inhibitor of NAMPT(24, 25), the rate limiting enzyme in the  
124 NAD<sup>+</sup> salvage biosynthetic pathway, led to significantly more neutral lipids at day 16  
125 (Figure 1A, day 16,  $P<0,01$ , Two-way ANOVA with Tukey's post-test), further reinforcing  
126 the idea that NAD<sup>+</sup> bioavailability might oppose lipogenesis. As it has been largely  
127 shown that SIRT1 is a mayor effector of NAD<sup>+</sup> signaling, we reasoned that it might be  
128 dispensable for adipogenesis. Surprisingly, selective inhibition of SIRT1 during  
129 adipogenic differentiation strongly hindered neutral lipid accumulation (Figure 1A, day  
130 16,  $P<0,01$ , Two-way ANOVA with Tukey's post-test). Interestingly, distinct dynamic  
131 changes in lipid accumulation were observed at days 4, 8 and 12 of adipogenic  
132 inductions with the different treatments (Figure 1A).

133 To further confirm that lipid accumulation is changing with the treatments in living cells  
134 while avoiding potential artifacts from fixation or ORO stain, we performed label-free  
135 Fluorescence lifetime microscopy of intrinsic lipid-associated fluorophores in living cells  
136 (see Methods section). Third harmonic generation (THG) images were used as  
137 reference to identify lipid droplets (26, 27) (Figure 1B, S1A, S1B), and they showed  
138 bright round dots for lipid droplets smaller than 1 $\mu$ m and hollow round structures at the  
139 interface between cytoplasm and lipid droplets larger than 1 $\mu$ m. FLIM images (Figure  
140 1B) indicated that lipid droplets associated fluorophores have a longer lifetime ( $\tau_m$ ) with  
141 respect to the rest of the cell cytoplasm, hence we determined a threshold to  
142 automatically and systematically identify and segment lipid droplets (Figure 1B, S1B,  
143 Methods section). This method allowed us to quantitatively assess lipid accumulation in  
144 live hMSCs during adipogenic induction (Figure 1C). We imaged cells at days 4, 6, 8  
145 and 12, corresponding to those when more dynamic changes were previously observed,  
146 and found that NAD<sup>+</sup> treatment significantly impaired lipid accumulation after day 8  
147 (Figure 1C, D; day 8 and 12,  $P < 0.001$ , Two way ANOVA with Tukey's post-test). With  
148 this approach, we didn't find significant differences in lipid accumulation in live cells  
149 when comparing FK866 and EX527 treatments to non-treated cells.

150 PPAR $\gamma$  is considered a master transcription factor for adipogenesis(28, 29). It's  
151 expression is induced in early stages(30), and sustains the specific transcriptional  
152 program for adipocyte differentiation(31). For these reasons, we explored how NAD<sup>+</sup>  
153 levels impact PPAR $\gamma$  protein expression during adipogenic induction of hMSCs (Figure  
154 1E, 1F). We found that PPAR $\gamma$ 1 isoform is strongly expressed since day 4 of  
155 differentiation for all tested conditions (Figure 1E, F). Yet, while its expression was

156 overall sustained along the adipogenic process in control cells, NAD<sup>+</sup> triggers a very  
157 significant reduction in PPAR<sub>γ</sub>1 protein expression while favoring expression of the  
158 PPAR<sub>γ</sub>2 isoform at differentiation day 8, which is lost at later stages (Figure 1E, F;  
159  $P < 0.01$ , Two-way ANOVA with Tukey's post-test). Interestingly, EX527 treatment led to  
160 significantly decreased expression of PPAR<sub>γ</sub>1 at the end of differentiation. Conversely,  
161 FK866 significantly increased PPAR<sub>γ</sub>2 isoform with respect to the control without  
162 affecting PPAR<sub>γ</sub>1 protein expression. As expected, a 16-days treatment of hMSC with  
163 any of the compounds led to detectable changes in PPAR<sub>γ</sub> expression (Figure S1C).  
164 Together, these differential dynamics on PPAR<sub>γ</sub> protein expression point to a mayor  
165 role for transcriptional control in the adipogenic potential shown after each treatment,  
166 which is also in line with the distinct outcomes in lipid accumulation.

### 167 **Extensive and specific reprogramming of the transcriptome during adipogenic** 168 **differentiation by NAD<sup>+</sup>**

169 To decipher the dynamic changes occurring in the transcriptome of hMSC during  
170 differentiation, we performed RNA-seq analyses from undifferentiated hMSC, and  
171 differentiated cells at two different time points: at 8 days of adipogenic differentiation  
172 (middle of differentiation protocol) and at 16 days (end of differentiation), in untreated  
173 cells and in cells treated with NAD<sup>+</sup>, FK866 or EX527. We first performed an unbiased  
174 principal component analysis (PCA) revealing that, as expected, the largest variation  
175 was due to the differentiation process (PC1, 24,92%; Figure 2A and S2A). Interestingly,  
176 the second component retaining 21.03% of the original variance between samples was  
177 mostly related to NAD<sup>+</sup> treatment (Figure 2A, S2A). Finally, a third component could be



178 due to the progress of the differentiation process itself (PC3, 8.98%; Figure 2A, S2A).  
179 We then performed differential gene expression analyses to compare between samples  
180 using DESeq2 (32), (see methods for details and Table S1 for normalized counts).  
181 These analyses further reinforced that NAD<sup>+</sup> treatment had a large impact in the  
182 transcriptome, comparable to the differentiation process itself, as more than 3000 genes  
183 were differentially expressed (DE) in differentiating cells treated with NAD<sup>+</sup> when  
184 compared with their untreated controls (adjusted  $P < 0.05$ ) (Figure S2B). Concomitantly,  
185 inhibition of NAD<sup>+</sup> biosynthesis by FK866 lead to just 171 differentially expressed genes  
186 when compared with the untreated controls at the end of the adipogenic process (Figure  
187 S2B, AD16\_FKvsAD16). Hence, we sought to determine the molecular signatures of  
188 NAD<sup>+</sup> treatment during adipogenic differentiation of hMSC. To do so, we first selected  
189 the transcripts specifically dysregulated by NAD<sup>+</sup> treatment and found 660 common DE  
190 genes in NAD<sup>+</sup> treated cells when compared with any other treatment or hMSC, which  
191 conform a unique NAD<sup>+</sup> molecular signature (Figure 2B). Out of these, 157 genes were  
192 consistently upregulated, while 407 were always silenced by the treatment (Figure 2B,  
193 Table S2). Next, we sought to explore the molecular routes responsible for the impaired  
194 adipogenic capacity of NAD<sup>+</sup> treated cells. Hence, we selected the genes which  
195 appeared consistently dysregulated in NAD<sup>+</sup> treated cells whAmong these, en  
196 compared with the rest of differentiating cells (AD, AD\_EX, AD\_FK). We identified 2,057  
197 of these genes at day 8 and 1,969 at day 16 after adipogenic induction. 993 genes were  
198 shared, out of which 70% (703) were consistently downregulated, while 28% (279) were  
199 always overexpressed (Figure 2C, 2D, Table S2). Gene ontology (GO) analyses  
200 revealed that most of the upregulated genes are implicated in apoptotic and response to

201 stress processes, while downregulated genes relate to mRNA metabolism, cellular  
202 motility, and differentiation processes (Figure 2E, 2F, Table S2). A subsequent pathway  
203 mapping in KEGG of the same transcripts revealed that many genes involved in steroid  
204 biosynthesis (*SQLE*, *DHCR7*, *FDFT1*, *SC5D*, *MSMO1*) were upregulated by NAD<sup>+</sup>  
205 treatment during adipogenic differentiation of hMSCs. Also, apoptotic signaling  
206 pathways appeared active, as suggested by the overexpression of several death  
207 receptors (*TNFRSF -10A*, *-10B*, *-10D*), probably triggered by activated ER stress and  
208 unfolded protein response, evidenced by increased transcription of *IRE1α (ERN1)*, BiP  
209 (*HSPA5*) and *XBP1* (Fig. 1G, Table S2). Interestingly, increased cholesterol  
210 biosynthesis induces ER stress in macrophages(33). In contrast, a unique set of genes  
211 downregulated by an excess of NAD<sup>+</sup> during adipogenic differentiation pertained to the  
212 ribosome pathway, involving many transcripts for ribosomal proteins (Figure 2H, S3A),  
213 indicating that their expression is strongly suppressed by NAD<sup>+</sup> in an adipogenic  
214 context. Additionally, many transcripts involved in cell adhesion and motility, which  
215 become expressed during differentiation, were downregulated in NAD<sup>+</sup> treated cells,  
216 indicating that the adipogenesis process is arrested. Furthermore, we found that the  
217 JAK-STAT pathway was impaired in NAD<sup>+</sup> treated cells, with downregulated transcripts  
218 including *STAT5A and STAT5B*, known positive regulators of the master adipogenic TF  
219 PPAR<sub>γ</sub> (34), or the leptin encoding gene *LEP* (Figure 2H, Table S2). Taken together,  
220 these data points towards NAD<sup>+</sup> promoting a proapoptotic and anti-adipogenic  
221 environment, therefore inhibiting differentiation and maturation of adipocytes.  
222 Accordingly, a promoter screening for transcription factor binding motifs revealed  
223 significant enrichment for SMAD motifs within promoters of upregulated genes (Figure

224 2I,  $P = 10^{-7}$ ), and for CEBP:AP1 motifs amongst downregulated genes' promoters  
225 (Figure 2J,  $P = 10^{-8}$ ). Indeed, SMADS are well known apoptotic regulators, while CEBP  
226 is a master adipogenic TF(29, 35).

227 **SIRT1 regulates terminal differentiation of pre-adipocytes but is dispensable for**  
228 **adipogenic commitment.**

229 If an excess of NAD<sup>+</sup> hinders the adipogenic transcriptional reprogramming, while  
230 inhibiting NAD<sup>+</sup> biosynthesis has only a mild transcriptional effect at the end of the  
231 adipogenic process, it is conceptually apparent that critical NAD<sup>+</sup> consuming enzymes  
232 such as SIRT1 would not be essential for adipocyte differentiation. Accordingly, SIRT1  
233 inhibition by EX527 had only a mild effect on the transcriptome at day 8, with just 57 DE  
234 genes compared with the untreated cells (Figure S2B, AD8\_EX vs AD8, Table S3).  
235 Strikingly, in terminally differentiated adipocytes we found 2040 differentially expressed  
236 genes, with 1095 upregulated and 945 downregulated transcripts (Figure S2B,  
237 AD16\_EX vs AD16, Figure 3A, Table S3). This is in line with the absence of lipid  
238 accumulation in these cells, and indicates that probably, SIRT1 is dispensable for  
239 lineage commitment, but essential for terminal differentiation of adipocytes.  
240 Interestingly, at day 8 of differentiation, the anti-adipogenic genes *EGR1* and *NR4A1*  
241 (36, 37) were overexpressed in EX527 treated cells (Table S3,  $P < 0,0001$ , Fold change  
242  $> 2$ ), and these have previously been shown to be upregulated in the early mitotic clonal  
243 expansion phase during preadipocyte differentiation(37), further reinforcing that SIRT1  
244 inhibition compromises maturation, but not commitment of preadipocytes. Accordingly,  
245 at day 16 many genes pertaining to pathways such as fatty acid metabolism,  
246 degradation or lipolysis were downregulated in cells treated with EX527, most of them

247 implicated in PPAR signaling (Figure 3B, S4A, Table S3). Amongst these, the adipokine  
248 genes leptin (*LEP*), leptin receptor (*LEPR*), and adiponectin (*ADIPOQ*) showed  
249 significantly lower levels in EX527 treated cells (Table S3). Interestingly, SIRT1  
250 inhibition upregulated transcripts enriched for adhesion and locomotion, critical  
251 processes during the onset of the adipogenesis, including the fibronectin gene *FN1*,  
252 which inhibits adipocyte maturation(38) (Figure 3C, S4B. Table S3). Accordingly, gene  
253 set enrichment analysis (GSEA) identified adipogenesis and apical junction as the top-  
254 ranked hallmarks enriched in untreated and EX527 treated cells respectively (Figure  
255 3D, E). Together, these data indicate that SIRT1 activity is essential for adipogenic  
256 differentiation, specifically by tightly controlling the transition between adipocyte  
257 commitment and maturation, and the maturation process itself. Remarkably, even  
258 though SIRT1 mRNA expression increased at the beginning of adipogenic induction  
259 (Figure 3F), the protein significantly increased after 8 days of adipogenic induction  
260 (Figure 3G,  $P < 0,0001$ , Kluskal-Wallis with Dunn's post-test), probably due to  
261 posttranscriptional regulation, and further reinforcing the notion that SIRT1 is essential  
262 for adipocyte maturation. Strikingly, a motif analysis revealed that pharmacological  
263 inhibition of SIRT1 downregulated preferred targets genes for distinct members of the  
264 FOX family of transcription factors (Figure 3H,  $P = 1E-11$ ), while overexpressed genes  
265 were enriched for motifs binding homeobox (NKX3-1,-2) or b-Helix- loop-helix (b-HLH)  
266 transcription factors such as CLOCK:BMAL (Figure 3I,  $P = 1E-8$ ). Indeed, most of these  
267 are well-known targets for SIRT1 deacetylation.

268 SIRT1 activity heavily relies on NAD<sup>+</sup> availability, hence the treatment with the NAMPT  
269 inhibitor FK866, known to dampen intracellular NAD<sup>+</sup> levels, would prevent SIRT1

270 activation and the subsequent adipocytic gene expression program. Surprisingly, FK866  
271 treatment during adipogenesis led to enhanced adipocytic differentiation, through  
272 overexpression of adipogenic hallmarks and increased adipocytokine and PPAR  
273 signaling over the control, non-treated adipocytes, at terminal differentiation (Figure  
274 4A,B, Table S4). Indeed, 39 genes involved in lipid metabolism, including *CD36*,  
275 *CEBPA*, *ADIPOQ*, *LPL*, *ACLY*, *FASN*, *ACACA*, *ACACB*, *PLIN1* and *RETSAT*, were  
276 highly expressed in terminal adipocytes treated with FK866 (Figure 4C). Moreover,  
277 genes related to ossification or cartilage development were downregulated in these cells  
278 (Figure 4D), indicating that low NAD<sup>+</sup> levels induced by FK866 treatment potentiate the  
279 adipogenic over the osteogenic lineage in hMSCs(7). This is in line with our previous  
280 observation that NAD<sup>+</sup> treatment hinders differentiation of hMSC to adipocytes; yet, it is  
281 in contrast with the need of SIRT1 activity, which relays on its cofactor NAD<sup>+</sup>, for  
282 adipocyte maturation. Furthermore, out of 57 differentially expressed genes between  
283 the control and EX527 treated cells at day 8 of differentiation, 33 (58%) were also  
284 dysregulated by FK866 treatment, suggesting that SIRT1 is not active in FK866 treated  
285 cells at day 8 (Figure 4E). Accordingly, SIRT1 expression both at the mRNA and protein  
286 levels was dampened by EX527 and FK866 to similar levels during adipogenic induction  
287 (Figure 4F, Two-way ANOVA with Turkey's post-test; Figure 4G, Kluskal-Wallis with  
288 Dunn's post-test; Figure S5A). These data suggest that SIRT1 function might be  
289 dispensable for adipocyte commitment, but necessary for differentiation, and the source  
290 of NAD<sup>+</sup> essential for SIRT1 activity does not require the salvage pathway.

291 **Increased NAD<sup>+</sup> bioavailability during the adipogenic process impairs the rise of**  
292 **mitochondrial respiration capacity in hMSCs.**

293 A major shift in metabolic phenotype is a hallmark of adipogenic differentiation. Hence,  
294 we investigated the functional effect of altering NAD<sup>+</sup> balance and SIRT1 activity during  
295 hMSC adipogenesis on energy metabolism by performing extracellular flux analysis for  
296 measuring cellular bioenergetics. As expected, non-treated hMSCs progressively  
297 increased their respiratory capacity during the adipogenic differentiation when  
298 compared to undifferentiated hMSCs, which retained low oxygen consumption rates  
299 across all tested days (Figure 5A-D). We observed that at day 4, all tested conditions  
300 retained low respiratory capacity, comparable to undifferentiated cells (Figure 5A), while  
301 the most prominent increase in respiration capacity occurs between days 8 to 16  
302 (Figure 5B-D). Indeed, FK866 treatment overall allowed the metabolic reprogramming  
303 during adipogenesis of hMSCs; however, NAD<sup>+</sup> treatment obstructed the progressive  
304 increase in mitochondrial respiration (Figure 5A-D). Interestingly, pharmacological  
305 inhibition of SIRT1 with EX527 showed major effect after day 12, consisting of markedly  
306 reduced respiratory capacity compared to the untreated cells. These results confirm that  
307 metabolic reprogramming during adipogenesis is compromised by SIRT1 inhibition  
308 specifically at late differentiation stages and reinforce the notion that SIRT1 is essential  
309 for adipocyte maturation. We observed major differences between treatments in  
310 maximal respiration and spare respiratory capacity at days 12 and 16, when induced  
311 cells either untreated or treated with FK866 showed a very significant increase  
312 compared to the rest of the conditions (Figure 5E-H,  $P < 0.0001$ , Two-way ANOVA with  
313 Tukey's post-test), indicating a high rate of oxidative phosphorylation in these cells.  
314 Non-mitochondrial respiration and proton leak did not show significant differences at  
315 any of the studied conditions (Figure S5). Notably, extracellular acidification rate

316 (ECAR) measurements revealed that undifferentiated hMSC exhibit a glycolytic  
317 phenotype, while treatment with NAD<sup>+</sup> during adipogenic induction also diminished the  
318 glycolytic flux (Figure 5I-L), indicating that these cells are metabolically less active.

319 Next, we performed label-free two-photon fluorescence lifetime microscopy (2P-FLIM)  
320 of the intrinsic metabolic biomarker NADH in live cells (see Methods section). We  
321 examined the fraction of bound NADH (fB\_NADH) during adipogenic differentiation with  
322 all treatments with a micrometer pixel resolution (Figure 6A). The results were in  
323 agreement with the extracellular flux analyses, and we saw that the fB\_NADH  
324 progressively increased during adipogenic differentiation, as a result of the metabolic  
325 shift from a glycolytic to an OXPHOS phenotype (Figure 6A, S6A-E). Also, NAD<sup>+</sup>  
326 treatment induced consistently low fB\_NADH across all tested days (Figure 6A),  
327 reinforcing the notion that increased NAD<sup>+</sup> bioavailability during adipogenic  
328 differentiation opposes the metabolic shift towards OXPHOS. With this approach, we  
329 only found significant reduction of fB\_NADH in cells treated with EX572 at the end of  
330 the differentiation process (Figure 6A), which is in line with the extracellular flux  
331 analyses indicating that SIRT1 inhibition hinders adipocytic maturation.

332 **Subcellular compartmentalization of NADH metabolism during adipogenesis**  
333 **depends on SIRT1 and is impaired by abnormally high NAD<sup>+</sup> levels.**

334 Our FLIM and extracellular flux analyses showed important disparities specifically for  
335 the cells treated with EX527 during adipogenic differentiation. Interestingly, at days 8  
336 and 12, two photon-FLIM didn't show significant differences between EX527 and  
337 untreated cells, while extracellular flux analyses indicated an important reduction in  
338 respiratory capacity of EX527-treated cells after day 8. For this reason, we ought to

339 determine the metabolic signatures at distinct subcellular compartments, in order to  
340 dissect<sup>i</sup> the subcellular location of the metabolic changes in these cells (see Methods  
341 section and Figure S1). This technique allowed us to capture intensity images and maps  
342 of fB\_ NADH in the entire cell and in different cellular compartments such as  
343 mitochondria and nucleus/cytoplasm, as shown in Figure 6B for a hMSC, and at day 8  
344 after adipogenic induction in untreated (AD) or NAD<sup>+</sup> treated cells (AD\_NAD<sup>+</sup>). Our  
345 single cell analysis at day 8 showed a wide distribution of cellular metabolic states in  
346 every culture condition (UD, AD, AD-NAD<sup>+</sup>, AD-FK866 or AD-EX527) (Figure 6D).  
347 Considering the metabolic fingerprint of the entire cell, NAD<sup>+</sup> treated cells showed lower  
348 fB\_ NADH than untreated cultures, while FK866 and EX527 treatments didn't show  
349 differences with untreated cells (Figure 6C, Two-way ANOVA with Tukey's post-test).  
350 Interestingly, we observed distinct subcellular compartmentalization of NADH  
351 metabolism depending on the treatment (Figure 6D, E). Consistently, fB\_ NADH at both  
352 mitochondria and nucleus/cytoplasm were lower in NAD<sup>+</sup> treated cells (Figure 6D-E).  
353 Moreover, the fB\_ NADH in the cytoplasm/nucleus was higher than in mitochondria in  
354 differentiating cells, while remained similar in hMSC; yet NAD<sup>+</sup> treatment showed an  
355 opposite ratio, where the mitochondrial fraction showed significantly higher levels of  
356 fB\_ NADH (Figure S6F). Interestingly, the fB\_ NADH of mitochondria appeared  
357 significantly decrease in cells treated with the SIRT1 inhibitor, while the fB\_ NADH  
358 increased within the nucleus/cytoplasm compartment in these cells when compared with  
359 the non-treated or with the FK866 treated cells (Figure 6D,E; P<0,05, Two-way ANOVA  
360 with Tukey's post-test). Together, our data reveal that energy metabolism progress  
361 during adipogenic differentiation is impeded by both SIRT1 inhibition and high NAD<sup>+</sup>



362 levels, through different mechanisms at distinct subcellular compartments. These  
363 observations have further implications for disease, as provide previously unappreciated  
364 sub-cellular insights into the previously reported efficacy of NAD<sup>+</sup> as a treatment for  
365 diet-induced obesity and metabolic dysfunction(39, 40).

366

## 367 **DISCUSSION**

368 In this study, we have demonstrated a previously unappreciated role for NAD<sup>+</sup>-SIRT1  
369 interplay in adipogenesis from hMSC which is dependent on the differentiation stage.  
370 We have shown that SIRT1 activity is essential for terminal adipocyte differentiation,  
371 and unexpectedly, NAD<sup>+</sup> availability fine tunes the adipogenic process. Mounting  
372 research demonstrates that SIRT1 inhibits adipogenesis in mesenchymal stem cells(41-  
373 47), however the dynamics of SIRT1 activity during adipogenesis remains poorly  
374 understood. Our gene expression data reveals that SIRT1 activity is dispensable for  
375 adipocyte commitment, as out of ~5,000 DE genes at day 8 of differentiation, less than  
376 60 were significantly altered between normally differentiating cells and those with  
377 inhibited SIRT1 activity. Unexpectedly, transition to mature adipocytes was strongly  
378 dampened by SIRT1 inhibition, demonstrating SIRT1 is essential. These results are in  
379 line with the notion that reducing SIRT1 activity specifically in fat could lead to improved  
380 metabolic function in obesity(48) . Moreover, in mice lacking SIRT1 specifically in MSC,  
381 their adipogenic capacity appears compromised leading to significant reduction in  
382 subcutaneous fat(49), further reinforcing this notion.

383 A number of studies report that the stem cell redox status is tightly regulated during  
384 differentiation, and thus activation of oxidative pathways constitute a metabolic  
385 signature of stem-cell differentiation(50, 51). Along the same lines, stem cells appear to  
386 contain lower levels of reactive oxygen species (ROS) than their mature progeny, and  
387 that ROS accumulation triggers intracellular signaling required for differentiation(52-55).  
388 Hence, it appears that metabolic reprogramming activates specific signaling cascades  
389 promoting either stem cell maintenance and self-renewal (reduced state) or stem cell  
390 proliferation and differentiation (oxidized state). Here, we have shown that fueling  
391 energy metabolism with NAD<sup>+</sup> markedly obstructs adipogenic differentiation. Imposing  
392 an oxidative redox state during early differentiation triggers a transcriptional program  
393 leading to translational arrest and induction of proapoptotic pathways, and these cells  
394 acquire a quiescent metabolic phenotype (Figure 2, 4). NAD<sup>+</sup> levels rise at late stages  
395 of differentiation(23), probably as a result of the increased oxidative metabolism which  
396 in our hMSC adipogenic differentiation model rapidly emerges between days 8-12  
397 (Figure 5, 6A). This is coincident with increased levels of SIRT1 transcription and  
398 protein expression (Figure 4F, 4G), reinforcing the idea of a SIRT1-dependent late  
399 stage of adipogenic differentiation. At this regard, obstructing the NAD<sup>+</sup> salvage  
400 pathway through constant inhibition of the rate-limiting enzyme NAMPT during  
401 adipogenesis didn't hinder the adipogenic capacity, demonstrating that the metabolic  
402 switch triggered by the transcriptional rewiring might control intracellular variations on  
403 NAD<sup>+</sup> levels and activity of NAD<sup>+</sup>- consuming enzymes. Indeed, we observed that  
404 NAMPT inhibition upregulated transcription of key lipid metabolism genes, and  
405 adipocytic identity at terminal differentiation (Figure 4A-C), thus favoring lipid

406 accumulation (Figure 1A). This suggests that the NAD<sup>+</sup> salvage pathway fine tunes  
407 adipogenesis in its late stages, and is in line with its protective role in diet-induced  
408 obesity(56, 57).

409 To gain insights into our observations in live, single cells at a submicrometric resolution,  
410 we developed a new method based on two-photon fluorescence lifetime microscopy  
411 (2P-FLIM) of intrinsic fluorophores that provides directly quantitative metrics of  
412 adipogenic stem cell differentiation, metabolic state of subcellular compartments. We  
413 measured a long lifetime of lipid droplets associated fluorophores (Figure 1B, 1C), as  
414 previously shown(58). We used the lifetime contrast to select autofluorescence from  
415 lipids and from NADH within cells (Figure S1A, S1B). Third harmonic generation  
416 microscopy was performed to visualize lipid droplets (26, 59) . Based on NADH intensity  
417 contrast, we also implemented an automated segmentation of mitochondria and  
418 cytoplasm/nuclear compartments that relies on their different concentration of NADH  
419 (Figure S1B). With this method, we observed lipid accumulation and increased fraction  
420 of bound NADH during adipogenic differentiation in live single cells, reflecting the  
421 metabolic shift from a glycolysis to OXPHOS metabolism during differentiation(60, 61).  
422 We provided here the first description of intracellular NADH metabolic signature in  
423 different subcellular compartments and at distinct stages of adipogenic differentiation in  
424 human cells, since subcellular characterisation of NAD<sup>+</sup>/NADH metabolism was  
425 previously demonstrated during few hours after adipogenic induction from 3T3-L1  
426 murine preadipocytes(62, 63). Our results show that spatial subcellular  
427 compartmentalisation of NADH metabolism is highly dependent on the differentiation  
428 stage and is intimately linked with the transcriptional reprogramming allowing progressive

429 lipid accumulation. Hereby, our observations are in agreement with the emerging view  
430 that temporal and spatial subcellular metabolic compartmentalisation contributes to  
431 numerous biological roles and regulation of intracellular signalling and transcription (24,  
432 64) and that NAD<sup>+</sup> compartmentalisation regulates adipogenesis(63).

433 Finally, the quantitative metrics based on fluorescence lifetime microscopy developed in  
434 this study serves as a label-free biomarker to simultaneously measure lipogenesis and  
435 metabolic shifts in single cell. Quantitative characterization of subcellular states from  
436 adipose tissues in health and disease using our two-photon microscopy-based method  
437 could provide means to uncover new roles of hMSC in obesity, thus paving the way for  
438 the development of MSC-based treatments.

439

#### 440 **ACKNOWLEDGEMENTS**

441 We thank all members of Aguilar-Arnal and Chiara Stringari laboratories for helpful  
442 discussions and advice. We thank Pierre Mahou, Isabelle Lamarre and Emmanuel  
443 Beaufrepaire for scientific discussions and technical help. We are thankful to Marcia  
444 Bustamante Zepeda, MSc, and Miguel Tapia Rodríguez, at the IIBo, for technical  
445 assistance. We are thankful to Dr. Alfonso Leon-del-Rio laboratory at the IIBo and  
446 particularly to Salvador Ramírez Jiménez, MSc, for kindly sharing reagents and  
447 equipment. This work was supported by Human Frontier Science Program (HFSP)  
448 under the contract RGY0078/2017 ChroMet to CS and LA-A, the Agence Nationale de  
449 la Recherche (ANR) under contracts ANR-10-INBS-04 France Biolmaging and ANR-11-  
450 EQPX-0029 Morphoscope2 to CS, and grant PAPIIT IN210619 from Universidad

451 Nacional Autónoma de México (UNAM) to LA-A. RO-S lab was supported by National  
452 Council of Science and Technology (CONACyT) (grants FC 2016/2672 and FOSISS  
453 272757). ES-R acknowledges the reception of PhD fellowship from CONACyT and the  
454 PhD program Doctorado en Ciencias Bioquímicas-UNAM.

455

#### 456 **AUTHOR'S CONTRIBUTION:**

457 LA-A and CS conceived and designed the study. ES-R, TPLU, XdT-R, GF-O conducted  
458 experiments. ES-R, TPLU, XdT-R, RO-S, CS and LA-A analyzed and interpreted the  
459 data. LN and AT assisted with Seahorse extracellular flux analyses. JJM provided  
460 hMSC and validated the model. Two-photon fluorescence lifetime microscopy was  
461 performed in CS lab and molecular biology and RNA-seq were done in LA-A lab. LA-A,  
462 CS, TPLU, ES-R and GF-O wrote the manuscript. All authors reviewed the manuscript.

463

#### 464 **DECLARATION OF INTEREST**

465 The authors declare that the research was conducted in the absence of any commercial  
466 or financial relationships that could be construed as a potential conflict of interest.

467

#### 468 **DATA AVAILABILITY**

469 All relevant data to this manuscript are available from the authors.

470

471 **METHODS**

472 **Isolation and characterization of BM-MSCs.** Bone marrow derived MSCs were  
473 obtained from healthy donors and have been previously described(65). Briefly,  
474 mononuclear cells (MNCs) from BM were obtained by density gradient centrifugation,  
475 and  $2 \times 10^5$  MNCs/cm<sup>2</sup> were seeded in low glucose Dulbecco's modified Eagle's medium  
476 (LG-DMEM, Gibco) with 10% fetal bovine serum (FBS; Gibco), 4mM L-glutamine and  
477 antibiotics. Cells were incubated at 37°C and 5% of CO<sub>2</sub>. At 80% of confluence,  
478 adherent cells were trypsinized and reseeded at a density of  $0.2 \times 10^4$  cells/cm<sup>2</sup>.  
479 Experiments were done at 3 - 5 passages. Cell surface markers expression of MSCs  
480 were determined by flow cytometry following our previously implemented and described  
481 protocols (65, 66), where MSCs were selected to express CD73, CD90 and CD105  
482 markers, while being negative to the hematopoietic markers CD45, CD34 and CD14  
483 (Figure S7A). Differentiation capacity was assessed using the StemPro™ Adipogenic  
484 and Osteogenic differentiation kits (Gibco A1007001, A1007201), and the Chondrogenic  
485 Differentiation Medium (Cambrex Bio Science) supplemented with 10 ng/ml of TGFβ  
486 (Peprotech 100-21C), following manufacturer's instructions. Adipogenic differentiation  
487 was evaluated by Oil Red O (Sigma O0625) staining after 16 days of induction,  
488 osteogenic differentiation was revealed by detecting alkaline phosphatase activity  
489 (Sigma B5655) after 14 days of induction, and chondrogenic differentiation was  
490 indicated by the presence of mucopolysaccharides positive to alcian blue (Sigma, ca.  
491 no. A5268), in micromasses cross-sections, after 28 days of induction(65, 66).  
492 Representative images are shown in Figure S7B.

493 All protocols were compliant with the Declaration of Helsinki and approved by the Ethics  
494 Committee of Villacoapa Hospital, Mexican Institute for Social Security (IMSS).  
495 Informed consent was given by the participants. Additionally, a BM-MSC line was  
496 purchased from ATCC .

497 **Cell culture and maintenance:** hMSCs were maintained in LG-DMEM (Gibco, cat. no.  
498 31600-034) supplemented with 10% FBS, 4mM L-glutamine, 100 µg/ml of penicillin and  
499 streptomycin (Gibco), and incubated at 37°C and 5% of CO<sub>2</sub>. Adipogenic differentiation  
500 was induced in MSCs in growing phase (70%-80% confluency), and drugs were present  
501 in the medium as indicated in the text and figures, following our previously standardized  
502 protocols(24). The medium and drugs were replaced every four days during the  
503 differentiation process. For live cell imaging, BM-hMSCs (ATCC) were cultured on 3.5-  
504 cm glass bottom petri dishes (MatTek, Ashland, MA, USA) in 2.5 ml LG-DMEM per well  
505 without phenol red and 10% FBS and 100 UI/mL penicillin and 100 µg/ml streptomycin.  
506 Cells were plated at the initial density of  $1,1 \times 10^4$  cells/cm<sup>2</sup> and allowed to attach  
507 overnight in a humidified cell culture incubator at 37 °C in 5% CO<sub>2</sub> before proceeding  
508 with treatments. During the imaging experiments, we replaced the adipogenic medium  
509 by basal medium without the phenol red before imaging. To determine the metabolic  
510 trajectory of NADH lifetime, MSCs were treated with rotenone 50 µM in DMSO (R8875;  
511 Sigma-Aldrich, St. Louis, MO, USA) and hydrogen peroxide (H<sub>2</sub>O<sub>2</sub>) 4mM in DMSO  
512 (216763; Sigma-Aldrich, St. Louis, MO, USA) to block the respiratory chain via complex  
513 I and to increase NAD<sup>+</sup>:NADH ratio via oxidative stress respectively. All cultures tested  
514 negative for mycoplasma contamination.

515 **Antibodies and reagents:** The antibodies used in this study are as follows: anti-SIRT1,  
516 Millipore cat. no. 07-131; anti-PPAR $\gamma$ , Cell Signaling, cat. no. 81B8; anti-GAPDH-HRP  
517 conjugated, GeneTex, cat. no. GTX627408-01; Goat anti-Rabbit Alexa Fluor® 594  
518 conjugated, Invitrogen cat. no. R37117; anti rabbit IgG-HRP conjugated, Invitrogen cat.  
519 no. 65-6120. All purchased antibodies were validated for mammalian studies (as shown  
520 on the manufacturers' websites). EX527 (E7034), FK866 (F8557) and NAD<sup>+</sup> (N8535)  
521 were purchased from Sigma.

522 **Oil-Red-O staining:** Cells grown on slides were briefly washed with PBS and fixed for  
523 45 min with 4% fresh paraformaldehyde. Preparation of Oil Red O (SIGMA, cat.  
524 no.O1391) working solution and staining of slides were performed as described(67).  
525 ORO was applied on the slides for 5 min at RT. Slides were washed twice during 10  
526 min. in water, and mounted in vectashield mounting media (Vector Labs, cat. no. H-  
527 1000). The images were captured with the camera AxioCam EEC 5s coupled to a ZEISS  
528 Primovert microscope, using a 20X magnification. Lipid droplets were quantified using  
529 the ImageJ software, by converting RGB to 8-bit grayscale images, and then using the  
530 "analyze particles" plug-in as described(68). Four frames per slide were used for image  
531 analyses and quantification (n=3 biological replicates with 4 technical replicates).

532 **Quantitative real-time PCR:** Total RNA was extracted from MSCs using TRIzol™  
533 Reagent (Invitrogen cat. no. 15596018) following the manufacturer's instructions. cDNA  
534 was obtained by retrotranscription of 1  $\mu$ g of total mRNA with iScript cDNA synthesis kit  
535 (Bio-Rad) according to the manufacturer's instructions. Real-time RT-PCR was done  
536 with the real-time CFX96 detection system (Bio-Rad). For a 10  $\mu$ l PCR reaction, 25 ng  
537 of cDNA template was mixed with the primers to final concentrations of 200 nM and



538 mixed with 5  $\mu$ l of iTaq<sup>TM</sup> Universal SYBR<sup>®</sup> Green Supermix kit (Bio-Rad). The  
539 reactions were done in triplicates with the following conditions: 30 sec at 95 °C, followed  
540 by 45 cycles of 30 s at 95 °C and 30 s at 60 °C. Expression levels were calculated using  
541 the ddCt method. The PCR primers were as follows: SIRT1: Fw, 5'-  
542 GCTGGAACAGGTTGCGGGAA-3'; Rv, 5'-GGGCACCTAGGACATCGAGGA-3'.  $\beta$ -  
543 actin: Fw, 5'-CTTGTACGCCAACACAGTGC-3'; Rv, 5'-ATACTCCTGCTTGCTGATCC-  
544 3'

545 **Immunofluorescences:** MSCs were seeded on Lab-Tek Chamber slides (Thermo  
546 Fisher) at  $9 \times 10^3$  cells/cm<sup>2</sup>. Cells were washed with phosphate buffered saline (PBS;  
547 Gibco), fixed with 1% of paraformaldehyde at 37°C for 10 min, washed twice with PBS  
548 and permeabilized with PBS 0.1% triton during 15 min. The slides were then washed  
549 with PBS, and incubated with blocking buffer (PBS, 0.1% Tween<sup>®</sup> 20, 2% BSA) for 1  
550 hour. Incubation with anti-SIRT1 (1:500) was performed over night at 4°C, and the  
551 secondary antibody (1:2,000) was incubated during 1 hour at RT. 1:5,000 dilution of  
552 Hoechst 33342 was used for nuclear counterstain (Invitrogen H1399) by incubating  
553 during 10 min at RT. Coverslips were mounted using VECTASHIELD<sup>®</sup> antifade  
554 mounting medium (Vector labs H1000) and sealed with nail polish. Fluorescence  
555 images were acquired by an Olympus DP70 Digital Camera in an Olympus BX51  
556 fluorescence microscope. Hoescht stain was acquired at a 1/300 s exposure, while  
557 SIRT1 intensity was acquired at 1/200 s. Densitometry was performed using ImageJ on  
558 3 cells at 4 different fields from 2 biological replicates.

559 **Western blotting.** MSCs were harvested from confluent 6-well dishes, washed with  
560 PBS and lysed with RIPA buffer supplemented with HDAC inhibitors (50mM Tris pH 8,

561 150mM NaCl, 1% 5mM EDTA pH8, 1% NP-40, 0.5% Na deoxycholate, and 0.1% SDS;  
562 all from Sigma). Cells were left on ice during 20 min. and centrifuged at 14,000 RPM  
563 during 15 min at 4°C. The protein extracts in the supernatants were snap frozen and  
564 stored at -80°C. Protein quantification was done using the Bradford colorimetric assay  
565 (Sigma B6916). 20µg of proteins were separated run on a 10% SDS-PAGE gel, at 100  
566 V for 2 hours using a mini-PROTEAN system (BIO-RAD) and transferred to  
567 nitrocellulose membrane (Millipore) at 40 mV overnight at 4°C. A 1:1,500 dilution of anti-  
568 PPAR $\gamma$  in blocking buffer (Tris-buffered saline plus Tween-20 -TBST- and 5% nonfat  
569 milk) was used to detect the protein. Antibodies to GAPDH protein at 1:20,000 dilution  
570 in PBST were used as a loading control. Proteins were revealed using  
571 chemiluminescent detection (Immobilon Western, Millipore WBKLS0100) and visualized  
572 using a Kodak GEL Logic 1500 Imaging System with Transilluminator.

573 **Extracellular flux analysis.** OCR and ECAR were measured using the Seahorse  
574 XFe96 Analyzer (Agilent), using The Cell Mito Stress Test Kit (Agilent, cat. no. 103015-  
575 100). MSCs were seeded at a density of 10,000 cells/well in a XF96 cell culture 96-well  
576 microplate (Agilent 101085-004) precoated with 10 µg/ml of fibronectin (Sigma F1141).  
577 Adipogenic induction and treatments were initiated after two days of seeding. One hour  
578 prior the Seahorse analysis, MSCs culture were washed with 200 µl/well of XF assay  
579 media supplemented with 10 mM glucose, 2mM glutamine and 1 mM pyruvate. Then,  
580 180 µl/well of this medium was added and the plate was equilibrated for 30 min at 37°C  
581 in a CO<sub>2</sub>-free incubator before being transferred to the Seahorse XFe96 analyzer.  
582 Measurement of OCR and ECAR was done at baseline and following sequential  
583 injections of (i) 2 µM oligomycin, an ATP synthase inhibitor, (ii) 0.5 µM carbonyl

584 cyanide-4-(trifluoromethoxy) phenylhydrazine (FCCP), a protonophoric uncoupler, and  
585 (iii) 0,5  $\mu$ M of rotenone, an inhibitor of complex I of the electron transport chain. Briefly,  
586 oligomycin inhibits mitochondrial ATP synthase, and the resulting drop in OCR and rise  
587 in ECAR are attributed to ATP-linked OCR and the compensation of glycolysis for the  
588 loss of mitochondrial ATP production. FCCP uncouples the mitochondrial proton  
589 gradient and oxygen consumption from ATP synthase, hereby driving maximal OCR.  
590 Rotenone inhibits complex I of the electron transport chain, hence it hinders  
591 mitochondrial oxygen consumption. Therefore, the residual OCR is regarded as  
592 nonmitochondrial.

593 **Expression profiling (RNA-seq) and analysis.** Total RNA from MSCs was extracted  
594 using Quick RNA MiniPrep Kit (Zymo Research, USA) following the manufacturer's  
595 instructions. RNA samples with RNA integrity number (RINs) > 7.0 were sent for library  
596 preparation and sequencing to Novogene Corporation Inc., California, USA. Briefly,  
597 mRNA was isolated using oligo(dT) beads and randomly fragmented by adding  
598 fragmentation buffer, followed by cDNA synthesis primed with random hexamers. Next,  
599 a second-strand synthesis buffer (Illumina), dNTPs, RNase H and DNA polymerase I  
600 were added for second-strand synthesis. After end repair, barcode ligation and  
601 sequencing adaptor ligation, the double-stranded cDNA library was completed with size  
602 selection to 250-300 bp, and PCR enrichment. Sequencing was performed on an  
603 Illumina NovaSeq 6000 Sequencing System with paired-end 150 bp reads, at 9 G raw  
604 data/sample. Total and mapped reads per sample are shown in Supplementary Table  
605 S1.

606 **RNA-seq data processing.** Human Reference genome and gene model annotation  
607 files were downloaded from genome website browser (NCBI/UCSC/Ensembl) directly.  
608 Indexes of the reference genome was built using STAR and paired-end clean reads  
609 were aligned to the *Homo sapiens* assembly GRCh38/hg38, with the STAR aligner v2.5  
610 (69). STAR uses the method of Maximal Mappable Prefix (MMP) which can generate a  
611 precise mapping result for junction reads. HTSeq v0.6.1 was used to count the read  
612 numbers mapped of each gene. Afterwards, FPKM of each gene was calculated based  
613 on the length of the gene and reads count mapped to it (70). Differential expression  
614 analysis between conditions (three biological replicates per condition) was performed  
615 with the DESeq2 R package (2\_1.6.3), which uses a model based on the negative  
616 binomial distribution (32). The resulting *P*-values were adjusted using the Benjamini and  
617 Hochberg's approach for controlling the False Discovery Rate (FDR). Genes with an  
618 adjusted *P*-value <0.05 were assigned as differentially expressed. The Venn diagrams  
619 were prepared using the function vennDiagram in R based on the gene list for different  
620 groups, or with Venny V 2.1 (<https://bioinfogp.cnb.csic.es/tools/venny/>). Differentially  
621 expressed genes were subjected to functional analyses using the "Compute Overlaps"  
622 tool to explore overlap with the CP (Canonical Pathways) and the GO:BP (GO biological  
623 process) gene sets at the MSigDB (molecular signature database). The tool is available  
624 at: <https://www.gsea-msigdb.org/gsea/msigdb/annotate.jsp>, and estimates statistical  
625 significance by calculating the FDR q-value. This is the FDR analog of the  
626 hypergeometric *P*-value after correction for multiple hypothesis testing according to  
627 Benjamini and Hochberg. Gene set enrichment analysis (GSEA) was performed using  
628 GSEA v. 4.0.3. (71) to determine the enrichment score within the Hallmark gene set

629 collection in MSigDB v7.0(72), selecting the Signal2Noise as the metric for ranking  
630 genes. The findMotifs.pl program in the HOMER software<sup>(73)</sup> was used for motif  
631 discovery and enrichment, searching within the genomic regions encompassing 300 Kb  
632 upstream and 50 Kb downstream the TSS, and selecting 6-8 bp for motif length. Motif  
633 enrichment is calculated by findMotifs.pl using the cumulative hypergeometric  
634 distribution.

635 All RNA-seq raw and processed data will be made publicly available at Gene  
636 Expression Omnibus (GEO) under the accession number GSE178615

637 **Two-photon excited fluorescence lifetime imaging (FLIM) and third harmonic**  
638 **generation (THG).** Imaging was performed on a laser scanning microscope  
639 (TriMScope, Lavisision Biotec, Germany). A simplified scheme of the multiphoton  
640 microscope is shown in Figure S7C. The Excitation is provided by a dual-output  
641 femtosecond laser (Insight DS++, Spectra-Physics, Santa Clara, CA, USA) with a first  
642 beam tunable from 680 nm to 1300 nm (120 fs pulses, 80 MHz) and a second, fixed  
643 wavelength beam at 1040 nm (200 fs pulses). A water Immersion objective (25X,  
644 NA=1.05, XLPLN-MP, Olympus, Japan) is used to focus the laser on the sample and  
645 collect fluoresce signal. Fluorescence signal is epi-detected by a hybrid photomultiplier  
646 tube (R10467U, Hamamatsu, Japan -), whereas and third-harmonic generation (THG)  
647 signal is forward detected by a photomultiplier (H6780-01, Hamamatsu, Japan). To  
648 perform Fluorescence lifetime microscopy of NADH, 760 nm wavelength excitation was  
649 used with a typical power of 12 mW (Figure S7D). A band-pass filter was used in front  
650 of the detector to collect NADH autofluorescence (Semrock FF01–460/80). Time-  
651 correlated single photon counting (TCSPC) electronics (Lavisision Biotec, Germany) with

652 5,5 ns dead time, and 27 ps time bins was used to measure the arrival time of the  
653 fluorescence photons with respect to the laser pulse and perform FLIM imaging. The  
654 laser trigger reference was taken from the fixed wavelength beam using a photodiode  
655 (PDA10CF-EC, Thorlab). Calibration of the FLIM system was performed by measuring  
656 the lifetime of fluorescein at pH=9 with a single exponential of 4 ns (Figure S7E). We  
657 measured the lifetime of free NADH in solution (Sigma Aldrich n. N8129, St. Louis, MO,  
658 USA) to calculate the fraction of bound NADH (Figure S6B). We typically collected 500  
659 photons for FLIM images of live cells with a pixel dwell time of 240  $\mu$ s/pixel and a total  
660 acquisition time on the order of one minute. Third harmonic generation was performed  
661 using a wavelength of 1100nm with a typical power of 12mW and the signal was  
662 collected with a band-pass filter (Semrock FF01–377/50) (Figure S7D). We typically  
663 collected 800 photons for THG images with a a pixel dwell time of 53  $\mu$ s/pixel and a total  
664 acquisition time of the order of one minute.

665 **Analysis of the Fluorescence Lifetime microscopy images.** Intensity images were  
666 analysed with Fiji-ImageJ (NIH, Bethesda, MD, USA). All FLIM data was processed and  
667 analysed with SimFCS (developed by the laboratory for Fluorescence Dynamics  
668 <https://www.lfd.uci.edu/globals/> ) and with a Matlab (Mathworks, Natick, MA, USA)  
669 custom written software. FLIM data were transformed by using FFT and plotted in the  
670 phasor plot as previously described (74) (75) (see Supplementary material). Briefly, the  
671 coordinates  $g$  and  $s$  in the phasor plot were calculated from the fluorescence intensity  
672 decay of each pixel of the image (Figure S7F) by using the transformations defined in  
673 the Supplementary material (equation 1 and 2). We applied an intensity threshold to  
674 eliminate the background of the cellular medium and a median filter on the  $g$  and  $s$

675 images to reduce the variance of the phasor location without decreasing the spatial  
676 resolution of the image. For every pixel of the image, we calculated the value of  $\tau_{\phi}$   
677 (equation (5) in Supplementary material) and  $\tau_m$  (equation (6) in Supplementary  
678 material) starting from the g and s images (Figure S1A). Fraction of bound NADH  
679 (equation (7) in Supplementary material) was graphically calculated as the distance  
680 from the experimental point to the location of free NADH (Figure S1A and Figure S6B).

681 **Subcellular segmentation of lipid droplets, cell NADH, mitochondria and nucleus**  
682 **and cytoplasm.** Image processing and segmentation was performed by a Matlab  
683 custom written software. The principles of the segmentation are illustrated in Figure  
684 S1B. A threshold (2.87 ns) was applied in the  $\tau_m$  lifetime image to automatically  
685 separate lipid droplets and NADH of the cell. Pixels with longer lifetime were assigned  
686 to a lipid mask while pixels with shorter lifetime were highlighted to the NADH cell mask.  
687 The  $\tau_m$  threshold was determined empirically to match the lipid mask border with the  
688 THG signal of the lipid droplet (Figure 1B). Then the mask of NADH cells was used to  
689 calculate  $fB\_NADH$  of the same ROI or cell. For quantification, we used the average  
690 values of  $fB\_NADH$  and lipid ratio. To quantify the lipid droplets in ROIs or in single  
691 cells, we calculated the ratio between the number of pixels of the lipid mask and the  
692 total number pixels of the cell: Single cell analysis was performed manually. We  
693 performed subcellular segmentation of mitochondria and nucleus plus cytoplasm  
694 applying a threshold (150 photons) to the intensity image multiplied with the NADH  
695 mask (Figure S1B). The threshold was determined based on the different  $NAD^+/NADH$   
696 ratios in mitochondria ( $\sim 10$ ) and cytoplasm and nucleus ( $\sim 50-1000$ )(76). Pixels with  
697 higher number of photons were assigned to mitochondria while pixels with lower

698 number of photons are assigned to nucleus and cytoplasm. The masks of mitochondria  
699 and nucleus and cytoplasm were applied to the map of fraction of bound NADH, and the  
700 average fraction of bound NADH was calculated in different cellular compartments for  
701 statistical analysis.

702 **Statistics and images analyses.** Data are shown as mean with SEM. Statistical  
703 analyses were performed using GraphPad Prism 8.2. The statistical tests were  
704 performed as indicated in the figure legends, mostly consisting of Two way ANOVA  
705 followed by Turkey's multiple comparisons test, or Kruskal–Wallis H test . Statistical  
706 significance was considered when the *P* value was <0.05. When possible, experimental  
707 evaluation was performed blind to the experimental conditions (i.e., specifically for  
708 western blot quantification, image processing and subsequent quantifications). Western  
709 blot analyses and image processing for overlay in different channels from  
710 immunofluorescences were performed with ImageJ software. Figures were arranged  
711 using Adobe Illustrator.

712

## 713 **BIBLIOGRAPHY**

- 714 1. Galic S, Oakhill JS, & Steinberg GR (2010) Adipose tissue as an endocrine organ. *Molecular and*  
715 *cellular endocrinology* 316(2):129-139.
- 716 2. Nguyen A, *et al.* (2016) Stromal vascular fraction: A regenerative reality? Part 1: Current  
717 concepts and review of the literature. *Journal of plastic, reconstructive & aesthetic surgery :*  
718 *JPRAS* 69(2):170-179.
- 719 3. Berry R & Rodeheffer MS (2013) Characterization of the adipocyte cellular lineage in vivo.  
720 *Nature cell biology* 15(3):302-308.
- 721 4. Rodeheffer MS, Birsoy K, & Friedman JM (2008) Identification of white adipocyte progenitor  
722 cells in vivo. *Cell* 135(2):240-249.
- 723 5. Cristancho AG & Lazar MA (2011) Forming functional fat: a growing understanding of adipocyte  
724 differentiation. *Nature Reviews Molecular Cell Biology* 12(11):722-734.
- 725 6. Peirce V, Carobbio S, & Vidal-Puig A (2014) The different shades of fat. *Nature* 510(7503):76-83.



- 726 7. Chen Q, *et al.* (2016) Fate decision of mesenchymal stem cells: adipocytes or osteoblasts? *Cell*  
727 *Death & Differentiation* 23(7):1128-1139.
- 728 8. Ghaben AL & Scherer PE (2019) Adipogenesis and metabolic health. *Nature Reviews Molecular*  
729 *Cell Biology* 20(4):242-258.
- 730 9. Morrison RF & Farmer SR (1999) Role of PPARgamma in regulating a cascade expression of  
731 cyclin-dependent kinase inhibitors, p18(INK4c) and p21(Waf1/Cip1), during adipogenesis. *The*  
732 *Journal of biological chemistry* 274(24):17088-17097.
- 733 10. Tontonoz P, Hu E, & Spiegelman BM (1994) Stimulation of adipogenesis in fibroblasts by PPAR $\gamma$ ,  
734 a lipid-activated transcription factor. *Cell* 79(7):1147-1156.
- 735 11. Tormos Kathryn V, *et al.* (2011) Mitochondrial Complex III ROS Regulate Adipocyte  
736 Differentiation. *Cell Metabolism* 14(4):537-544.
- 737 12. Shyh-Chang N, Daley GQ, & Cantley LC (2013) Stem cell metabolism in tissue development and  
738 aging. *Development* 140(12):2535-2547.
- 739 13. Cantó C, *et al.* (2012) The NAD<sup>+</sup> precursor nicotinamide riboside enhances oxidative metabolism  
740 and protects against high-fat diet-induced obesity. *Cell metabolism* 15(6):838-847.
- 741 14. Gariani K, *et al.* (2016) Eliciting the mitochondrial unfolded protein response by nicotinamide  
742 adenine dinucleotide repletion reverses fatty liver disease in mice. *Hepatology* 63(4):1190-1204.
- 743 15. Trammell SAJ, *et al.* (2016) Nicotinamide Riboside Opposes Type 2 Diabetes and Neuropathy in  
744 Mice. *Scientific Reports* 6(1):26933.
- 745 16. Remie CME, *et al.* (2020) Nicotinamide riboside supplementation alters body composition and  
746 skeletal muscle acetylcarnitine concentrations in healthy obese humans. *The American journal*  
747 *of clinical nutrition* 112(2):413-426.
- 748 17. Gulshan M, *et al.* (2018) Overexpression of Nmnat3 efficiently increases NAD and NGD levels  
749 and ameliorates age-associated insulin resistance. *Aging Cell* 17(4):e12798.
- 750 18. Liu S, Kim T-H, Franklin DA, & Zhang Y (2017) Protection against High-Fat-Diet-Induced Obesity in  
751 MDM2<sup>C305F</sup> Mice Due to Reduced p53 Activity and Enhanced Energy Expenditure.  
752 *Cell Reports* 18(4):1005-1018.
- 753 19. Yoshino J, Mills KF, Yoon MJ, & Imai S (2011) Nicotinamide mononucleotide, a key NAD(+)   
754 intermediate, treats the pathophysiology of diet- and age-induced diabetes in mice. *Cell*  
755 *Metabolism* 14(4):528-536.
- 756 20. Jukarainen S, *et al.* (2016) Obesity is associated with low NAD<sup>+</sup>/SIRT pathway expression in  
757 adipose tissue of BMI-discordant monozygotic twins. *The Journal of Clinical Endocrinology*  
758 101(1):275-283.
- 759 21. Chang H-C & Guarente L (2014) SIRT1 and other sirtuins in metabolism. *Trends in Endocrinology*  
760 *& Metabolism* 25(3):138-145.
- 761 22. Giblin W, Skinner ME, & Lombard DB (2014) Sirtuins: guardians of mammalian healthspan.  
762 *Trends in Genetics* 30(7):271-286.
- 763 23. Okabe K, *et al.* (2020) NAD<sup>+</sup> Metabolism Regulates Preadipocyte Differentiation by Enhancing  $\alpha$ -  
764 Ketoglutarate-Mediated Histone H3K9 Demethylation at the PPAR $\gamma$  Promoter. *Frontiers in Cell*  
765 *and Developmental Biology* 8(1409).
- 766 24. Aguilar-Arnal L, *et al.* (2016) Spatial dynamics of SIRT1 and the subnuclear distribution of NADH  
767 species. *Proceedings of the National Academy of Sciences* 113(45):12715-12720.
- 768 25. Hasmann M & Schemainda I (2003) FK866, a highly specific noncompetitive inhibitor of  
769 nicotinamide phosphoribosyltransferase, represents a novel mechanism for induction of tumor  
770 cell apoptosis. *Cancer research* 63(21):7436-7442.
- 771 26. Chang T, *et al.* (2013) Non-invasive monitoring of cell metabolism and lipid production in 3D  
772 engineered human adipose tissues using label-free multiphoton microscopy. *Biomaterials*  
773 34(34):8607-8616.

- 774 27. Débarre D, *et al.* (2006) Imaging lipid bodies in cells and tissues using third-harmonic generation  
775 microscopy. *Nature methods* 3(1):47-53.
- 776 28. Lefterova MI, Haakonsson AK, Lazar MA, & Mandrup S (2014) PPAR $\gamma$  and the global map of  
777 adipogenesis and beyond. *Trends in Endocrinology & Metabolism* 25(6):293-302.
- 778 29. Lefterova MI, *et al.* (2008) PPAR $\gamma$  and C/EBP factors orchestrate adipocyte biology via adjacent  
779 binding on a genome-wide scale. *Genes & Development* 22(21):2941-2952.
- 780 30. Aprile M, *et al.* (2014) *PPARG* in Human Adipogenesis: Differential Contribution of  
781 Canonical Transcripts and Dominant Negative Isoforms. *PPAR Research* 2014:537865.
- 782 31. Tontonoz P & Spiegelman BM (2008) Fat and Beyond: The Diverse Biology of PPAR $\gamma$ . *Annual*  
783 *Review of Biochemistry* 77(1):289-312.
- 784 32. Love MI, Huber W, & Anders S (2014) Moderated estimation of fold change and dispersion for  
785 RNA-seq data with DESeq2. *Genome Biology* 15(12):550.
- 786 33. Feng B, *et al.* (2003) The endoplasmic reticulum is the site of cholesterol-induced cytotoxicity in  
787 macrophages. *Nature cell biology* 5(9):781-792.
- 788 34. Gurzov EN, Stanley WJ, Pappas EG, Thomas HE, & Gough DJ (2016) The JAK/STAT pathway in  
789 obesity and diabetes. *The FEBS Journal* 283(16):3002-3015.
- 790 35. Conery AR & Luo K (2006) Smad Proteins in Apoptotic and Survival Signaling. *Smad Signal*  
791 *Transduction*, (Springer), pp 113-129.
- 792 36. Boyle KB, *et al.* (2009) The transcription factors Egr1 and Egr2 have opposing influences on  
793 adipocyte differentiation. *Cell Death Differ* 16(5):782-789.
- 794 37. Zhang Y, *et al.* (2018) Targeting nuclear receptor NR4A1-dependent adipocyte progenitor  
795 quiescence promotes metabolic adaptation to obesity. *J Clin Invest* 128(11):4898-4911.
- 796 38. Liu J, *et al.* (2005) Changes in integrin expression during adipocyte differentiation. *Cell*  
797 *Metabolism* 2(3):165-177.
- 798 39. Connell NJ, Houtkooper RH, & Schrauwen P (2019) NAD<sup>+</sup> metabolism as a target for metabolic  
799 health: have we found the silver bullet? *Diabetologia* 62(6):888-899.
- 800 40. Yoshino J, Baur JA, & Imai SI (2018) NAD(+) Intermediates: The Biology and Therapeutic Potential  
801 of NMN and NR. *Cell Metab* 27(3):513-528.
- 802 41. Bäckesjö CM, Li Y, Lindgren U, & Haldosén LA (2006) Activation of Sirt1 decreases adipocyte  
803 formation during osteoblast differentiation of mesenchymal stem cells. *Journal of bone and*  
804 *mineral research : the official journal of the American Society for Bone and Mineral Research*  
805 21(7):993-1002.
- 806 42. Li Y, *et al.* (2011) Nicotinamide phosphoribosyltransferase (Nampt) affects the lineage fate  
807 determination of mesenchymal stem cells: a possible cause for reduced osteogenesis and  
808 increased adipogenesis in older individuals. *Journal of bone and mineral research : the official*  
809 *journal of the American Society for Bone and Mineral Research* 26(11):2656-2664.
- 810 43. Peltz L, *et al.* (2012) Resveratrol exerts dosage and duration dependent effect on human  
811 mesenchymal stem cell development. *PLoS one* 7(5):e37162.
- 812 44. Puri N, *et al.* (2012) Heme induced oxidative stress attenuates sirtuin1 and enhances  
813 adipogenesis in mesenchymal stem cells and mouse pre-adipocytes. *Journal of cellular*  
814 *biochemistry* 113(6):1926-1935.
- 815 45. Song J, *et al.* (2019) Nicotinamide mononucleotide promotes osteogenesis and reduces  
816 adipogenesis by regulating mesenchymal stromal cells via the SIRT1 pathway in aged bone  
817 marrow. *Cell Death & Disease* 10(5):336.
- 818 46. Tseng PC, *et al.* (2011) Resveratrol promotes osteogenesis of human mesenchymal stem cells by  
819 upregulating RUNX2 gene expression via the SIRT1/FOXO3A axis. *Journal of bone and mineral*  
820 *research : the official journal of the American Society for Bone and Mineral Research*  
821 26(10):2552-2563.

- 822 47. Zhou Y, *et al.* (2015) SIRT1 inhibits adipogenesis and promotes myogenic differentiation in  
823 C3H10T1/2 pluripotent cells by regulating Wnt signaling. *Cell & Bioscience* 5(1):61.
- 824 48. Mayoral R, *et al.* (2015) Adipocyte SIRT1 knockout promotes PPAR $\gamma$  activity, adipogenesis and  
825 insulin sensitivity in chronic-HFD and obesity. *Molecular metabolism* 4(5):378-391.
- 826 49. Simic P, *et al.* (2013) SIRT1 regulates differentiation of mesenchymal stem cells by deacetylating  
827  $\beta$ -catenin. *EMBO Mol Med* 5(3):430-440.
- 828 50. Folmes Clifford DL, *et al.* (2011) Somatic Oxidative Bioenergetics Transitions into Pluripotency-  
829 Dependent Glycolysis to Facilitate Nuclear Reprogramming. *Cell Metabolism* 14(2):264-271.
- 830 51. Folmes Clifford DL, Dzeja Petras P, Nelson Timothy J, & Terzic A (2012) Metabolic Plasticity in  
831 Stem Cell Homeostasis and Differentiation. *Cell Stem Cell* 11(5):596-606.
- 832 52. Yanes O, *et al.* (2010) Metabolic oxidation regulates embryonic stem cell differentiation. *Nature*  
833 *chemical biology* 6(6):411-417.
- 834 53. Tsatmali M, Walcott EC, & Crossin KL (2005) Newborn neurons acquire high levels of reactive  
835 oxygen species and increased mitochondrial proteins upon differentiation from progenitors.  
836 *Brain research* 1040(1-2):137-150.
- 837 54. Ito K, *et al.* (2004) Regulation of oxidative stress by ATM is required for self-renewal of  
838 haematopoietic stem cells. *Nature* 431(7011):997-1002.
- 839 55. Smith J, Ladi E, Mayer-Proschel M, & Noble M (2000) Redox state is a central modulator of the  
840 balance between self-renewal and differentiation in a dividing glial precursor cell. *Proceedings of*  
841 *the National Academy of Sciences of the United States of America* 97(18):10032-10037.
- 842 56. Stromsdorfer Kelly L, *et al.* (2016) NAMPT-Mediated NAD<sup>+</sup> Biosynthesis in Adipocytes Regulates  
843 Adipose Tissue Function and Multi-organ Insulin Sensitivity in Mice. *Cell Reports* 16(7):1851-  
844 1860.
- 845 57. Wang L-F, *et al.* (2017) Inhibition of NAMPT aggravates high fat diet-induced hepatic steatosis in  
846 mice through regulating Sirt1/AMPK $\alpha$ /SREBP1 signaling pathway. *Lipids in Health and Disease*  
847 16(1):82.
- 848 58. Datta R A-GA, Cinco R, Gratton E. (2015) Fluorescence lifetime imaging of endogenous  
849 biomarker of oxidative stress. *Sci Rep.* 20(5):9848.
- 850 59. Débarre D, *et al.* (2006) Imaging lipid bodies in cells and tissues using third-harmonic generation  
851 microscopy. *Nat Methods.* 3(1):47-53.
- 852 60. Liu Z, Pouli, D, Alonzo, CA, Varone, A, Karaliota, S, Quinn, KP, Münger, K, Karalis, KP,  
853 Georgakoudi I. (2018) Mapping metabolic changes by noninvasive, multiparametric, high-  
854 resolution imaging using endogenous contrast. *Sci Adv.* 7(4):3.
- 855 61. Meleshina AV DV, Shirmanova MV, Shcheslavskiy VI, Becker W, Bystrova AS, Cherkasova EI,  
856 Zagaynova EV. (2016) Probing metabolic states of differentiating stem cells using two-photon  
857 FLIM. *Sci Rep.* 6:21853.
- 858 62. Li D ZW, Qu JY. (2008) Time-resolved spectroscopic imaging reveals the fundamentals of cellular  
859 NADH fluorescence. *Opt Lett.* 33(20):2365-2367.
- 860 63. Ryu KW, *et al.* (2018) Metabolic regulation of transcription through compartmentalized NAD<sup>+</sup>  
861 biosynthesis. *Science* 360(6389):eaan5780.
- 862 64. Cambronne XA & Kraus LW (2020) Location, Location, Location: Compartmentalization of NAD<sup>+</sup>  
863 Synthesis and Functions in Mammalian Cells. *Trends in Biochemical Sciences* 45(10): 858-873
- 864 65. Fajardo-Orduna GR, *et al.* (2016) Bone Marrow Mesenchymal Stromal Cells from Clinical Scale  
865 Culture: In Vitro Evaluation of Their Differentiation, Hematopoietic Support, and  
866 Immunosuppressive Capacities. *Stem cells and development* 25(17):1299-1310.
- 867 66. Castro-Manreza ME, *et al.* (2014) Human mesenchymal stromal cells from adult and neonatal  
868 sources: a comparative in vitro analysis of their immunosuppressive properties against T cells.  
869 *Stem cells and development* 23(11):1217-1232.

- 870 67. Mehlem A, Hagberg CE, Muhl L, Eriksson U, & Falkevall A (2013) Imaging of neutral lipids by oil  
871 red O for analyzing the metabolic status in health and disease. *Nature Protocols* 8(6):1149-1154.  
872 68. Collins TJ (2007) ImageJ for microscopy. *BioTechniques* 43(1 Suppl):25-30.  
873 69. Dobin A, *et al.* (2012) STAR: ultrafast universal RNA-seq aligner. *Bioinformatics* 29(1):15-21.  
874 70. Mortazavi A, Williams BA, McCue K, Schaeffer L, & Wold B (2008) Mapping and quantifying  
875 mammalian transcriptomes by RNA-Seq. *Nature methods* 5(7):621-628.  
876 71. Subramanian A, *et al.* (2005) Gene set enrichment analysis: A knowledge-based approach for  
877 interpreting genome-wide expression profiles. *Proceedings of the National Academy of Sciences*  
878 102(43):15545-15550.  
879 72. Liberzon A, *et al.* (2015) The Molecular Signatures Database (MSigDB) hallmark gene set  
880 collection. *Cell systems* 1(6):417-425.  
881 73. Heinz S, *et al.* (2010) Simple combinations of lineage-determining transcription factors prime cis-  
882 regulatory elements required for macrophage and B cell identities. *Molecular cell* 38(4):576-589.  
883 74. Chiara Stringari AC, Olivier Cinquin, Michelle A. Digman, Peter J. Donovan, Enrico Gratton (2011)  
884 Phasor approach to fluorescence lifetime microscopy distinguishes different metabolic states of  
885 germ cells in a live tissue. *PNAS*:13582-13587.  
886 75. Suman Ranjit LM, David M. Jameson, Enrico Gratton (2018) Fit-free analysis of fluorescence  
887 lifetime imaging data using the phasor approach. *Nature Protocols*:pages1979–2004.  
888 76. Stein LR & Imai S (2012) The dynamic regulation of NAD metabolism in mitochondria. *Trends in*  
889 *endocrinology and metabolism: TEM* 23(9):420-428.

890

891

892 **FIGURE LEGENDS:**

893 **Figure 1: NAD<sup>+</sup> hinders adipogenic differentiation and lipid accumulation in**  
894 **hMSC.**

895 Adipogenic differentiation was induced in hMSC in the absence or presence of the  
896 indicated drugs: NAD<sup>+</sup> (5 mM), FK866 (1 nM) or the SIRT1-specific inhibitor EX527 (50  
897  $\mu$ M). **A)** Neutral lipids were stained with Oil-Red-O (ORO) at the indicated days after  
898 adipogenic induction, and representative images from are shown. Quantification was  
899 performed by densitometry from n=4 technical and 3 biological replicates. **B)**  
900 Representative images from Label free quantification of lipid droplets by Fluorescence  
901 Lifetime Microscopy of an adipocyte at terminal differentiation. Intensity , modulation  
902 lifetime  $\tau_m$  ( $\tau_m$ ) lipid mask determined by a  $\tau_m$  threshold, and Third harmonic  
903 generation (THG) intensity are shown as indicated. The graph on the right shows a  
904 cross sectional profile of lipid mask created by a  $\tau_m$  threshold and THG signal of one  
905 lipid droplet of 5  $\mu$ m diameter. **C)** Representative images of intensity (left), modulation  
906 lifetime  $\tau_m$  (middle) and lipid mask (right) of hMSCs during adipogenic differentiation at  
907 the indicated days of culture under selected treatments **D)** Quantification from lipid ratio  
908 at indicated days and treatments during the differentiation process of hMSC. n=14  
909 single cells; experiments were conducted in triplicate. **E)** PPAR $\gamma$ 1 and PPAR $\gamma$ 2 protein  
910 expression levels were measured by western blot in whole cell extracts at the indicated  
911 days after adipogenic induction. p84 was used as loading control. **F)** quantification of  
912 PPAR $\gamma$ 1 and PPAR $\gamma$ 2 protein expression, normalized to p84 loading control. n=3  
913 biological replicates. For all graphs, data is presented by mean  $\pm$  SEM (\*p< 0,05, \*\*p<  
914 0,01, \*\*\*p< 0,001, Two-way ANOVA with Tukey's post-test)

915 **Figure 2: NAD<sup>+</sup> treatment during adipogenesis from hMSC induces profound and**  
916 **specific changes in the transcriptome.**

917 RNA-seq was performed per triplicate from multipotent hMSC (MSC, UD0), or at days 8  
918 (AD8) and 16 (AD16) after adipogenic induction in the absence (AD8, AD16) or  
919 presence of 5 mM NAD<sup>+</sup> (AD8\_NAD, AD16\_NAD), 1 nM FK866 (AD8\_FK866,  
920 AD16\_FK866) or 50  $\mu$ M EX527 (AD8\_EX527, AD16\_EX527) **A)** Principal component  
921 analysis (PCA) was computed for the whole data. **B)** Heatmap comparing expression  
922 from 660 genes DE exclusively in NAD<sup>+</sup> treated cells (FDR-adjusted *P*-value <0.05) **C)**  
923 Overlap of DE transcripts between NAD<sup>+</sup> treated cells and the rest of the tested  
924 conditions at day 8 and day 16 after adipogenic induction **D)** Heatmap comparing  
925 expression from 994 genes DE exclusively in NAD<sup>+</sup> treated cells at both days 8 and 16  
926 after adipogenic induction when compared with the rest of the samples. **E-H)** Functional  
927 annotation of the 994 DE genes constituting the NAD<sup>+</sup> transcriptional signature:  
928 biological processes (E, F) or KEGG pathways (G-H) for consistently upregulated (E, G)  
929 or downregulated (F, H) transcripts. **I, J)** Homer *de novo* motif discovery analyses from  
930 promoters of genes specifically upregulated (I) or downregulated (J) after NAD<sup>+</sup>  
931 treatment during adipogenic induction.

932 **Figure 3: SIRT1 activity is essential for terminal differentiation of pre-adipocytes.**

933 **A)** Heatmap comparing expression from 2040 genes DE between EX527-treated cells  
934 (50  $\mu$ M) and untreated cell at day 16 after adipogenic induction on hMSC. (FDR-  
935 adjusted *P*-value <0.05) **B, C)** KEGG pathway enrichment analyses from genes  
936 downregulated (B) or upregulated (C) by EX527 treatment during adipogenic

937 differentiation, at day 16 after induction, compared with untreated, terminally  
938 differentiated adipocytes. **D, E**) Gene set enrichment analysis (GSEA) investigated  
939 within the molecular signature database (MSigDB) “Hallmark” gene set collection.  
940 Genes were rank-ordered by differential expression between terminally differentiated  
941 adipocytes untreated (AD16) or treated with EX527 (AD16\_EX). **F**) *SIRT1* gene  
942 expression levels were assessed by RT-qPCR at the indicated days after adipogenic  
943 induction on hMSC. n= 3 biological and 2 technical replicates. One-way ANOVA  
944 followed by Tukey’s post test. \* p <0.05, \*\* p <0.01, \*\*\* p <0.001. Symbol key for  
945 multiple comparisons: \*: day 0 vs days 3, 6; \$: day 0 vs days 9-16; #: days 3, 6 vs days  
946 9-16. **G**) *SIRT1* protein expression and subcellular location was explored by  
947 immunofluorescence at the indicated days after adipogenic induction on hMSC. Boxplot  
948 shows densitometric analyses from n= 2 biological and 7 technical replicates. Kluskal-  
949 Wallis test followed by Dunn's multiple comparisons test was applied. \* p <0.05, \*\* p  
950 <0.01, \*\*\* p <0.001. **H, I**) Homer *de novo* motif discovery analyses from promoters of  
951 genes downregulated (H) or upregulated (I) by EX527 treatment during adipogenic  
952 induction, at terminal differentiation (day 16).

#### 953 **Figure 4: The NAD<sup>+</sup> salvage pathway is dispensable for adipogenesis**

954 **A**) Gene set enrichment analysis (GSEA) was investigated within the molecular  
955 signature database (MSigDB) “Hallmark” gene set collection. Genes were rank-ordered  
956 by differential expression between terminally differentiated adipocytes untreated (AD16)  
957 or treated with 1 nM FK866 (AD16\_FK). **B**) Functional annotation (Biological processes  
958 and KEGG pathways) for 144 genes upregulated by FK866 treatment during  
959 adipogenesis, at terminal adipogenic differentiation (day 16). **C**) Heatmap comparing

960 expression levels between the indicated samples at day 16 from 39 genes involved in  
961 lipid metabolism. **D)** Biological processes enriched in 44 genes downregulated by  
962 FK866 treatment during adipogenesis, at terminal differentiation (day 16). **E)** Overlap of  
963 DE genes (up- or downregulated) comparing EX527 and FK866 treated cells during  
964 adipogenic induction, at day 8 **F)** *SIRT1* gene expression levels were assessed by RT-  
965 qPCR at the indicated days after adipogenic induction on hMSC either untreated (AD)  
966 or treated with the indicated drugs. n= 3 biological and 2 technical replicates. One-way  
967 ANOVA followed by Tukey's post test. \*\* p <0.01, \*\*\* p <0.001. **G)** Boxplot showing  
968 *SIRT1* protein levels analyzed by immunofluorescence at days 8 and 16 after  
969 adipogenic induction on hMSC. Cells were either untreated (AD), or treated with the  
970 indicated compounds. Densitometric analyses are from n= 2 biological and 7 technical  
971 replicates. Kluskal-Wallis test followed by Dunn's multiple comparisons test was applied.  
972 n.s.: non-significant \* p <0.05, \*\* p <0.01, \*\*\* p <0.001.

973 **Figure 5: NAD<sup>+</sup> impairs mitochondrial bioenergetics during adipogenic induction**  
974 **in hMSC.**

975 Analysis of oxygen consumption rate (OCR) and extracellular acidification rate (ECAR)  
976 was performed using Seahorse XF analyzer to assess mitochondrial respiration and  
977 lactate production from n = 3 biological replicates with 6-10 technical replicates each. **A-**  
978 **D)** OCR was measured at days 4 (A), 8 (B), 12 (C) or 16 (D) after adipogenic induction  
979 in hMSC, in the absence or presence of the indicated treatments. with sequential  
980 addition of oligomycin (Oligo, complex V inhibitor), FCCP (a protonophore), and  
981 Rotenone/antimycin A (Rot/AA, complex III inhibitor), **E-F)** Mitochondrial bioenergetic  
982 parameters calculated from extracellular flux analyses: basal respiration, maximal



983 respiratory capacity, spare respiratory capacity, and ATP production. Two-way ANOVA  
984 followed by Tukey's post test. \*  $p < 0.05$ , \*\*  $p < 0.01$ , \*\*\*  $p < 0.001$ . **I-L**) ECAR was  
985 measured after serial addition of oligomycin and FCCP. Data is presented by mean  
986  $\pm$ SEM.

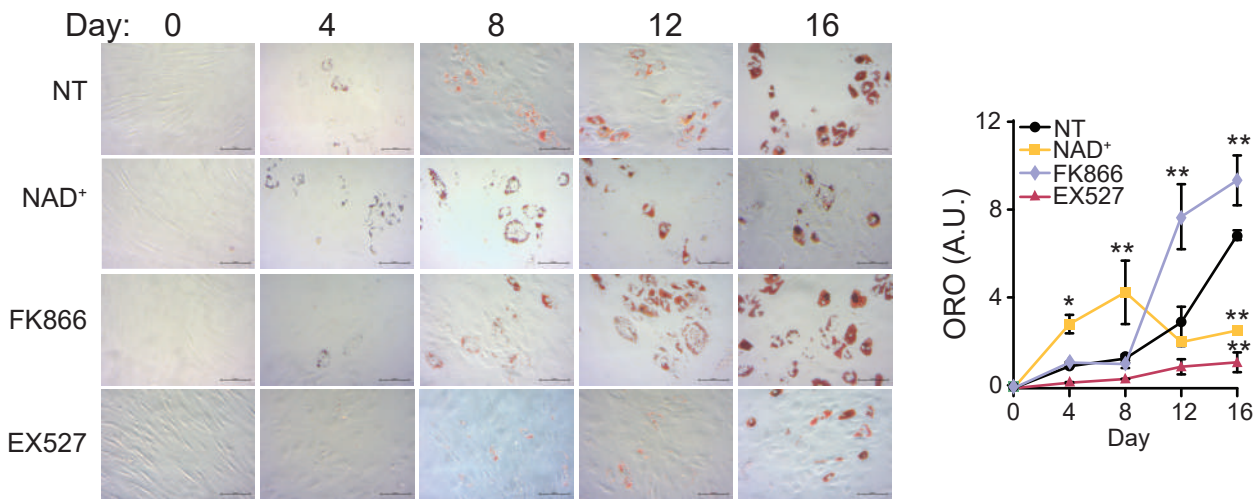
987 AD: adipogenic induced cells; NAD<sup>+</sup> adipogenic induced cells treated with 5 mM NAD<sup>+</sup>;  
988 FK866: adipogenic induced cells treated with 1 nM FK866; EX527: adipogenic induced  
989 cells treated with 50  $\mu$ M EX527. MSC: untreated, undifferentiated hMSC.

990 **Figure 6: Subcellular compartmentalization of NADH metabolism during**  
991 **adipogenesis depends on SIRT1 activity.**

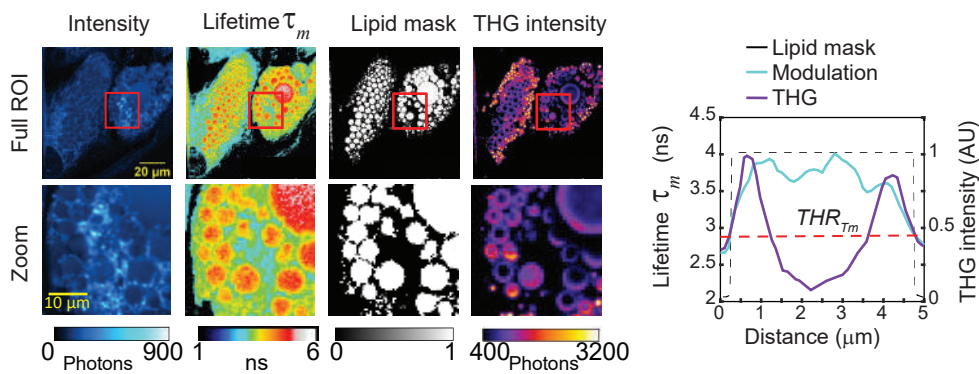
992 **A)** Representative images of fraction of bound NADH (fB\_NADH) of hMSCs during  
993 adipogenic differentiation at days 4, 6, 8, 12 and 16 of induction in the absence (NT) or  
994 presence of the indicated treatments: 5 mM NAD<sup>+</sup>, 1 nM FK866 or 50  $\mu$ M EX527. Low  
995 fB\_NADH (blue colors) corresponds to a cellular glycolytic phenotype, while high  
996 fB\_NADH (red colors) corresponds to an OXPHOS phenotype. Quantification of fraction  
997 of bound NADH in each culture condition was performed from  $n = 14$  single cells.  
998 Experiments were conducted per triplicate. Data is presented by mean  $\pm$ SEM. **B)**  
999 Representative images of intensity and fB\_NADH of hMSCs, pre-adipocytes (AD) and  
1000 cells treated with NAD<sup>+</sup> during adipogenic induction (AD\_NAD<sup>+</sup>) imaged at day 8 of  
1001 differentiation, show different spatial distributions of fraction of bound NADH in different  
1002 cell compartments such as mitochondria, nucleus and cytoplasm. **C-E)** Quantification of  
1003 fB\_NADH in single cells at day 8 from hMSC (MSC), pre-adipocyte (AD) and cells treated  
1004 with the indicated compounds during adipogenic differentiation. Quantification from  $n =$   
1005 63-125 cells was performed in the whole cell (C), or the mitochondrial (D) and

- 1006 nuclear/cytoplasmic (E) subcellular compartment. Two-way ANOVA followed by  
1007 Tukey's post test. \*  $p < 0.05$ , \*\*  $p < 0.01$ , \*\*\*  $p < 0.001$ , n.s.: non-significant.

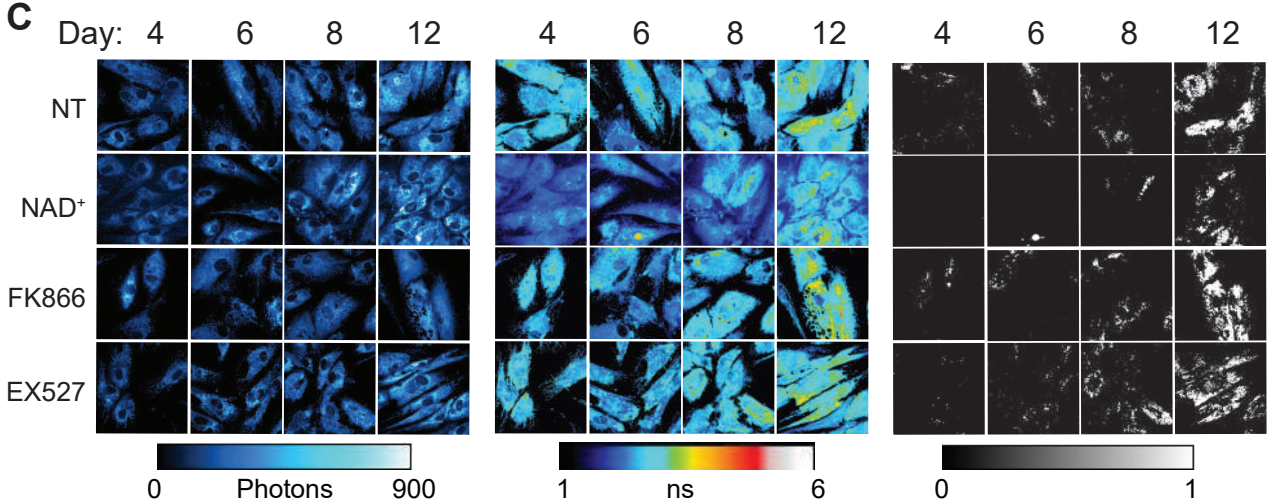
**A**



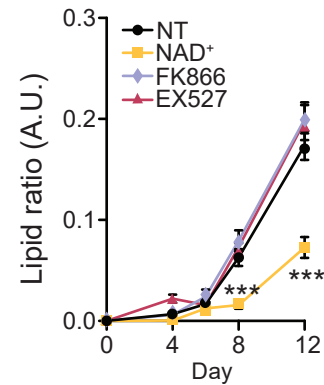
**B**



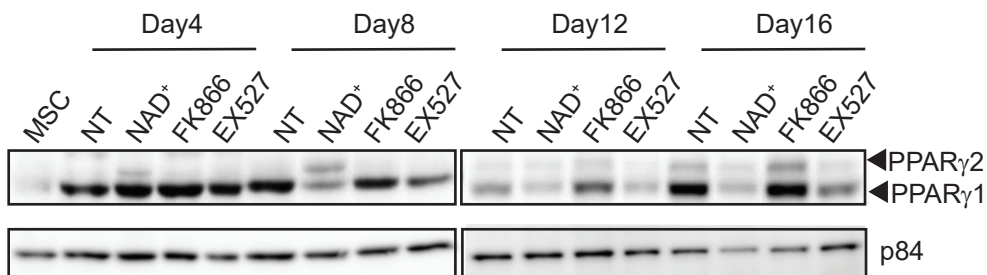
**C**



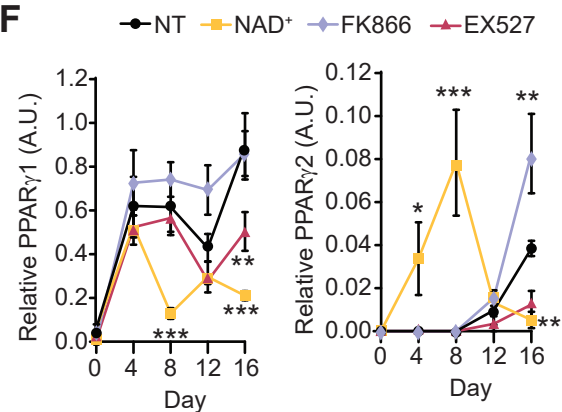
**D**



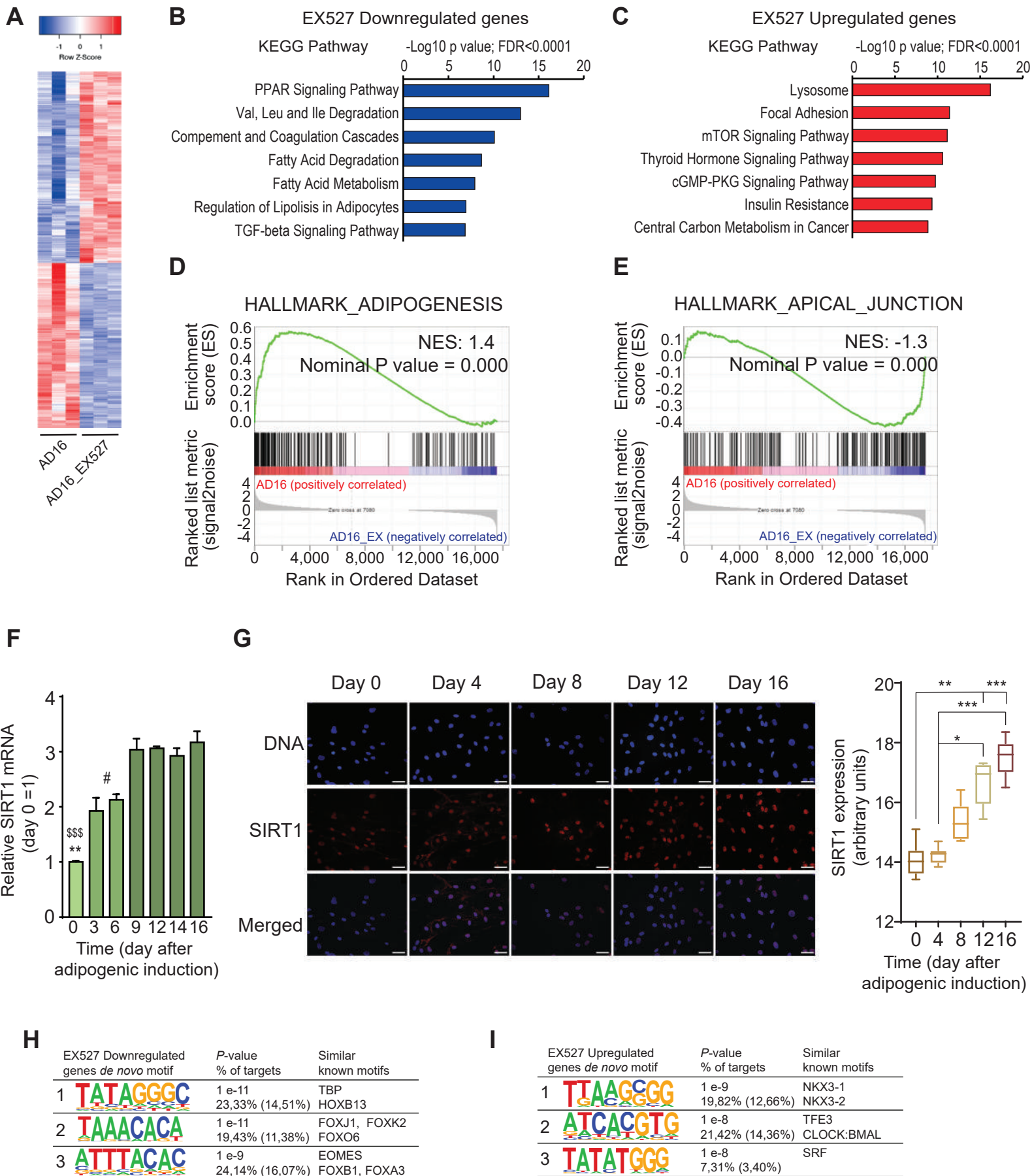
**E**

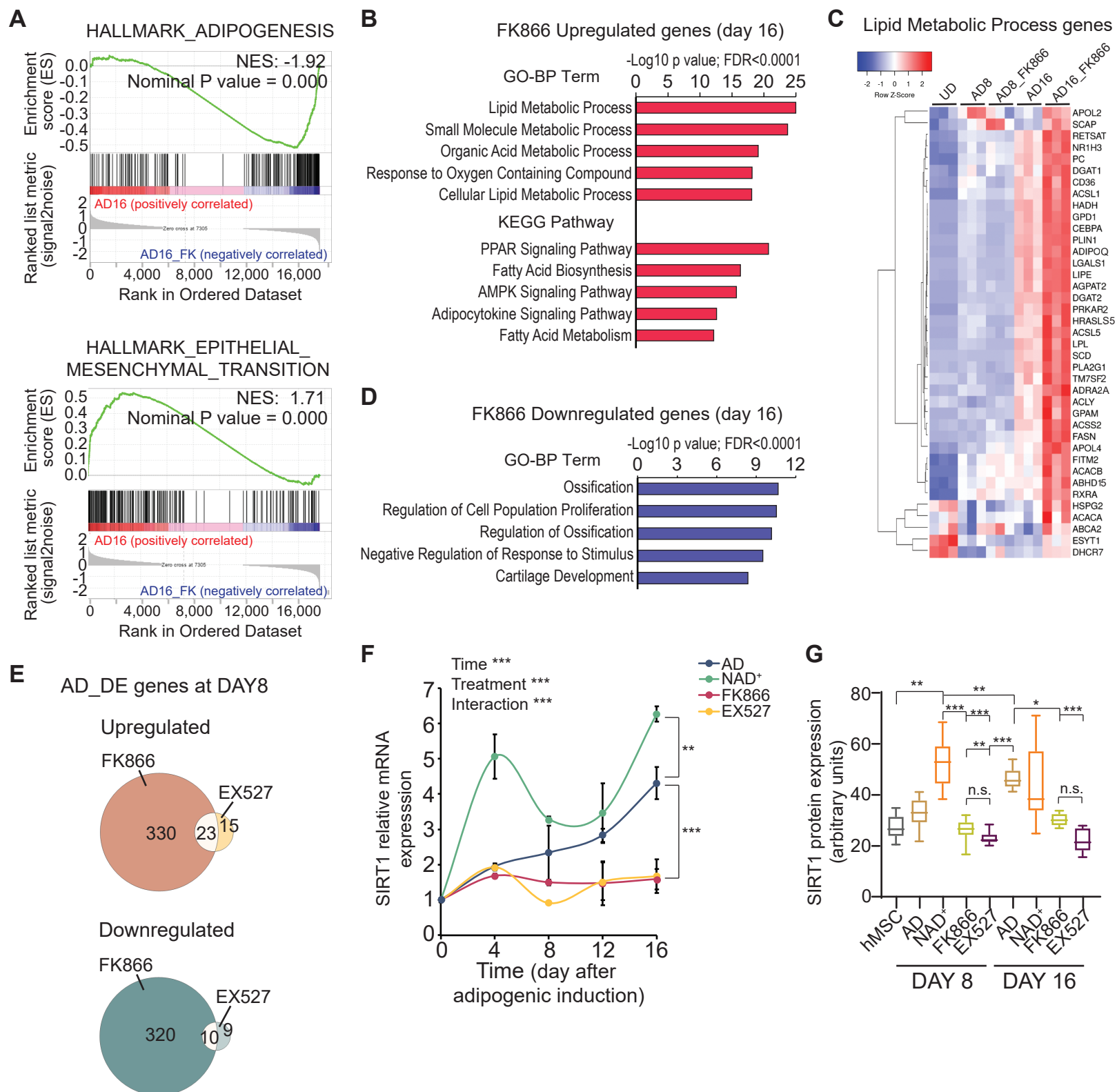


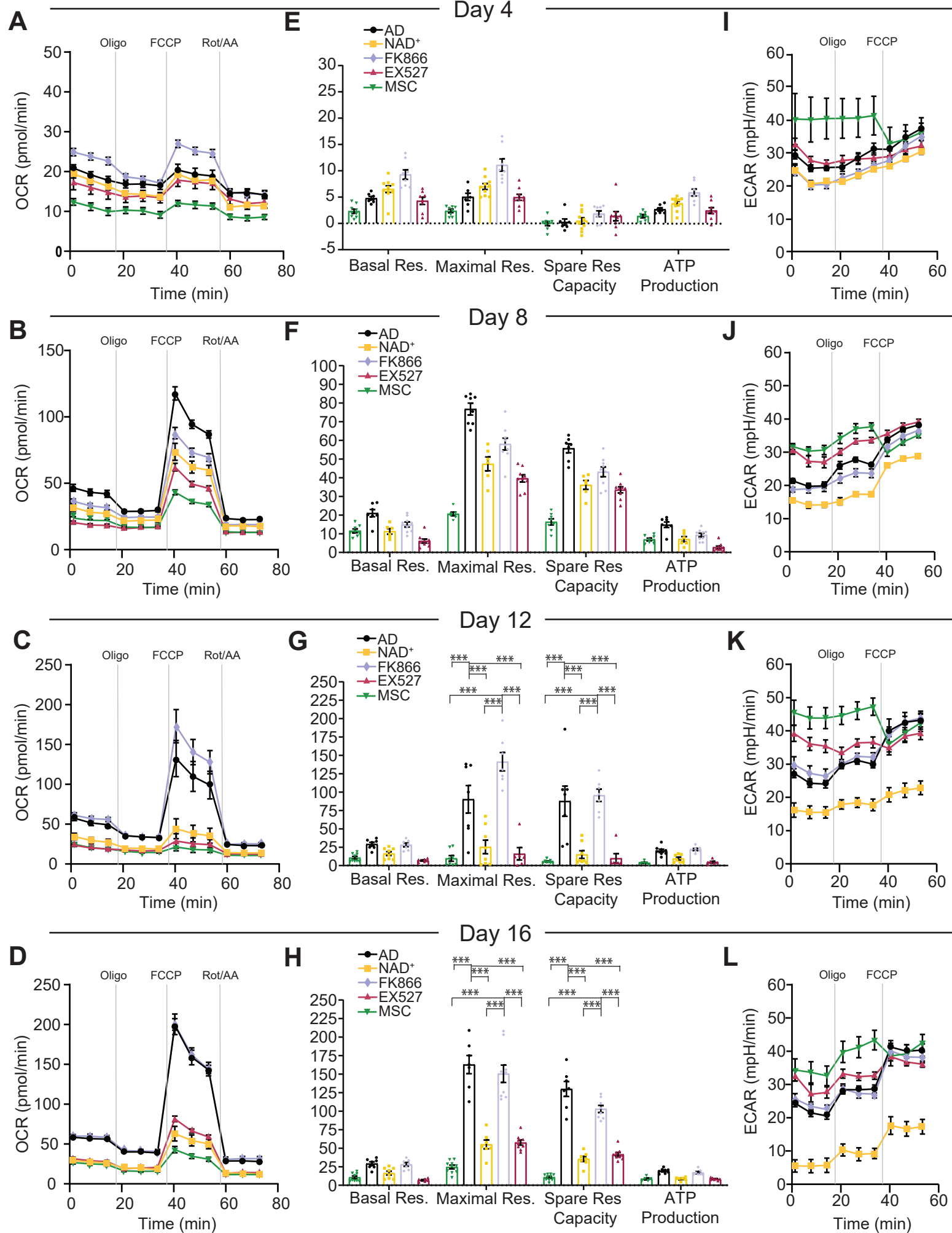
**F**



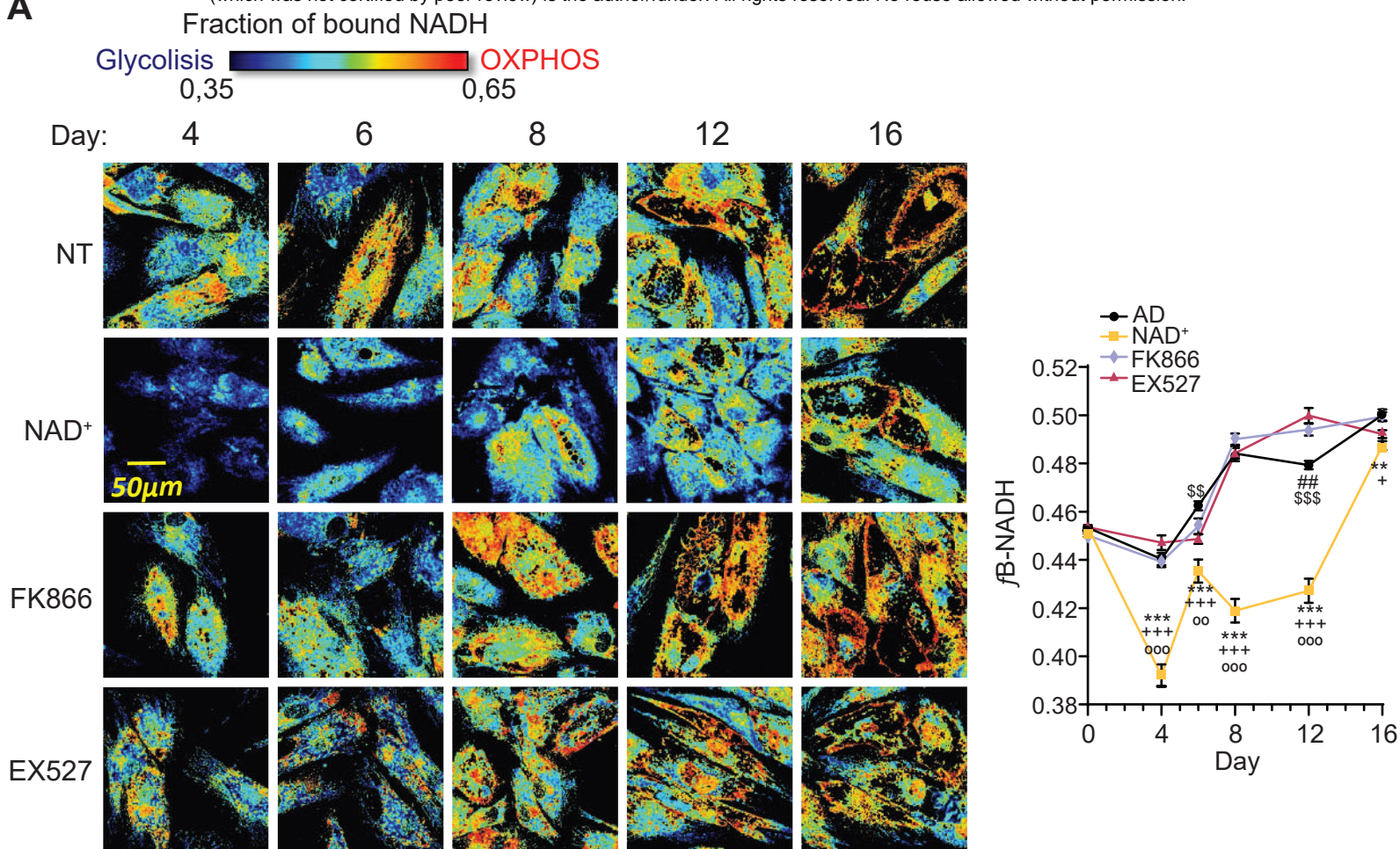




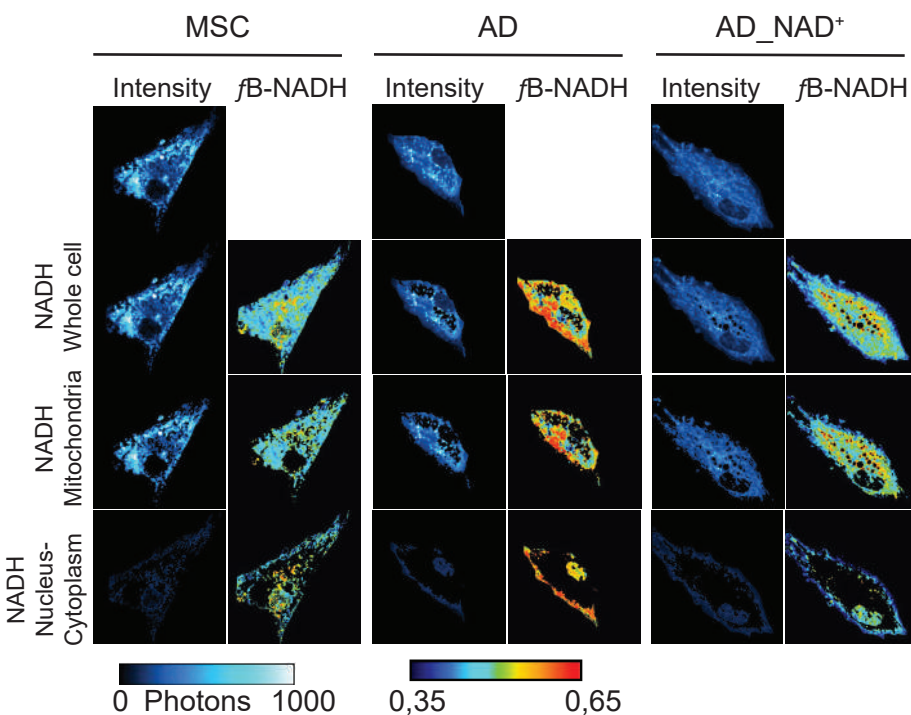




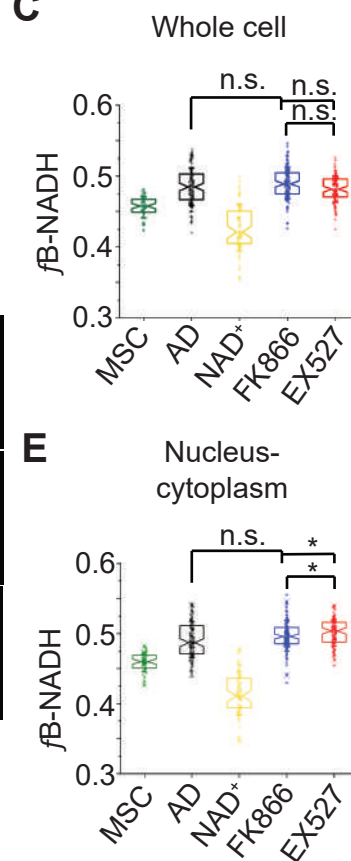
**A**



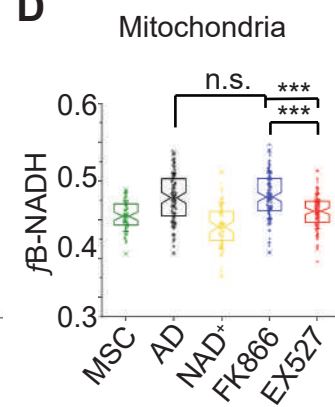
**B**



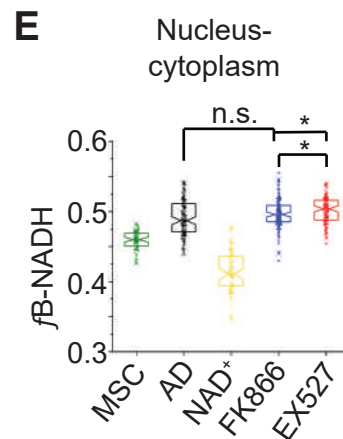
**C**



**D**



**E**





## **Supplementary Information for**

### **Coordination between metabolic transitions and gene expression by NAD<sup>+</sup> availability during adipogenic differentiation in human cells.**

Edgar Sanchez-Ramírez, Thi Phuong Lien Ung, Ximena del Toro-Rios, Guadalupe R. Fajardo-Orduña, Lilia G. Noriega, Armando R. Tovar, Juan José Montesinos, Ricardo Orozco-Solís, Chiara Stringari and Lorena Aguilar-Arnal.

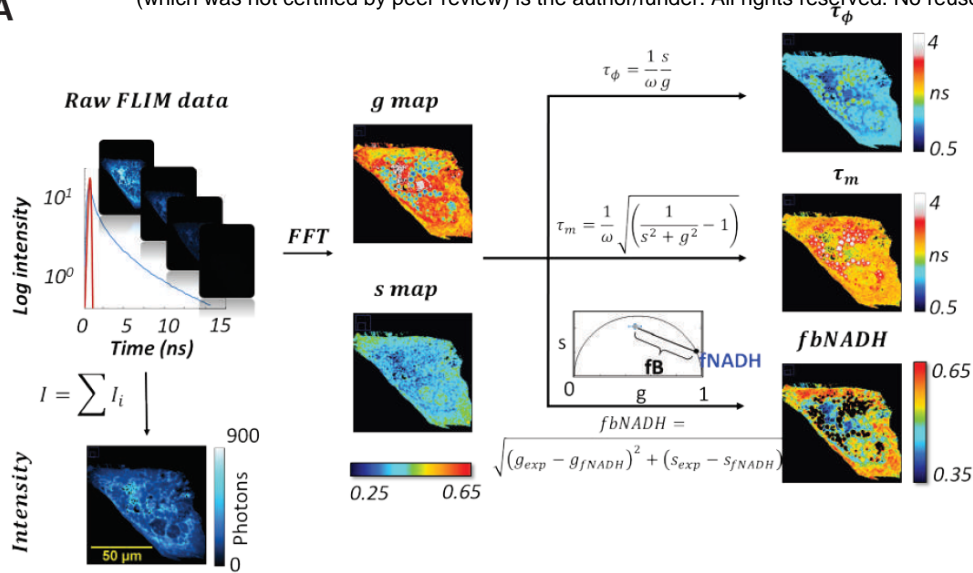
Corresponding author: Chiara Stringari

Email: [chiara.stringari@polytechnique.edu](mailto:chiara.stringari@polytechnique.edu)

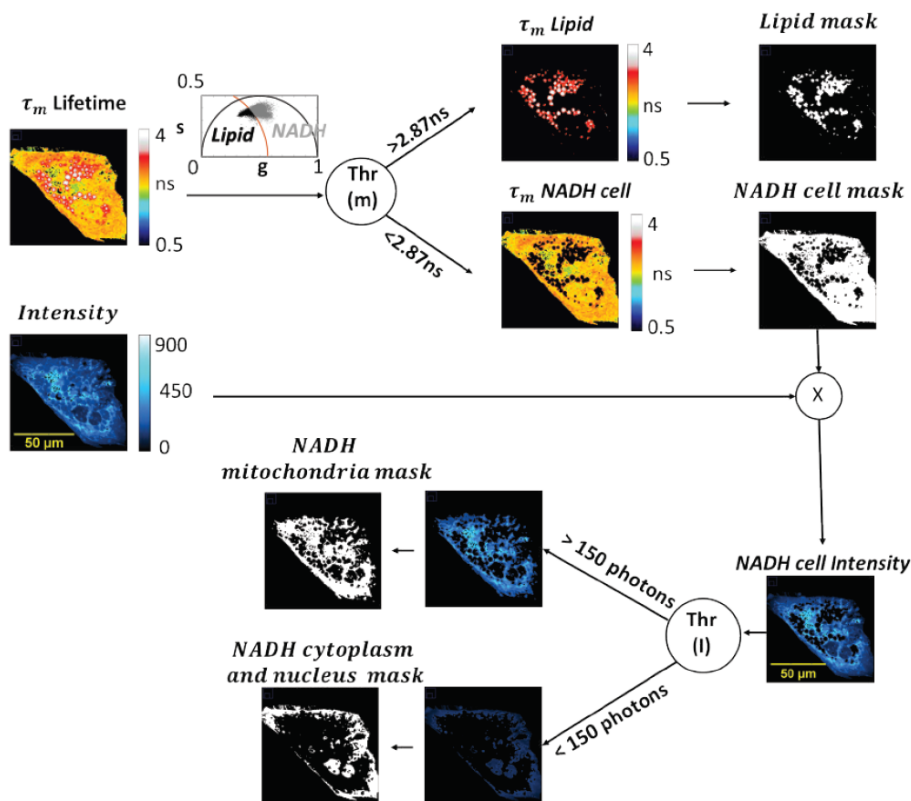
Corresponding author: Lorena Aguilar-Arnal

Email: [loreaguilararnal@iibiomedicas.unam.mx](mailto:loreaguilararnal@iibiomedicas.unam.mx)

**A**



**B**



**C**

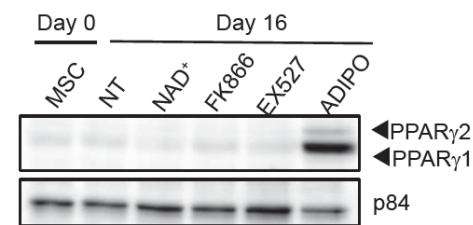
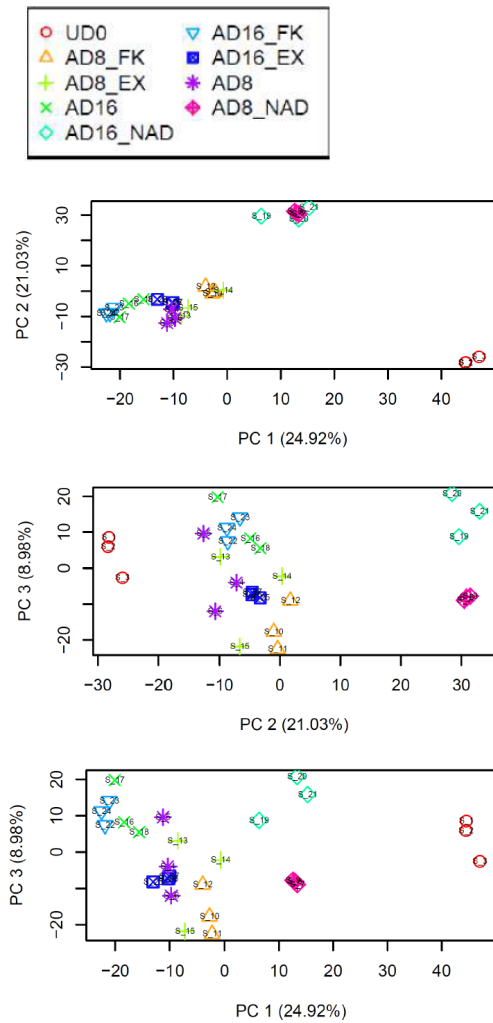


**Fig. S1. Image processing workflow for FLIM and Lipid and NADH segmentation** **A)** Workflow of FFT based Phasor analysis of Fluorescence Lifetime Microscopy images. **B)** Workflow of sub-cellular segmentation based on lifetime and intensity thresholds. A threshold on modulation lifetime (THR (m) = 2.87ns) is applied to separate lipid droplets and NADH in entire cell. The pixels of the FLIM image with  $\tau_m > \text{THR (m)}$  (black points in the phasor plot) are assigned to lipid droplets while the pixels with  $\tau_m < \text{THR (m)}$  (grey points in the phasor plot) are assigned to the NADH signal in the rest of the cell. A threshold (150 photons) on intensity of cell NADH is applied to segment mitochondria and nucleus plus cytoplasm. The pixels with intensity  $> \text{THR (I)}$  are assigned to mitochondria while pixels with Intensity  $< \text{THR (I)}$  are assigned to the cytoplasm and nucleus. **C)** PPAR $\gamma$ 1 and PPAR $\gamma$ 2 protein expression levels were measured by western blot in whole cell extracts from hMSC untreated (NT) or treated with the indicated compounds for 16 days. Terminally differentiated adipocytes (ADIPO) were also included. p84 was used as loading control.

**A**



**B**

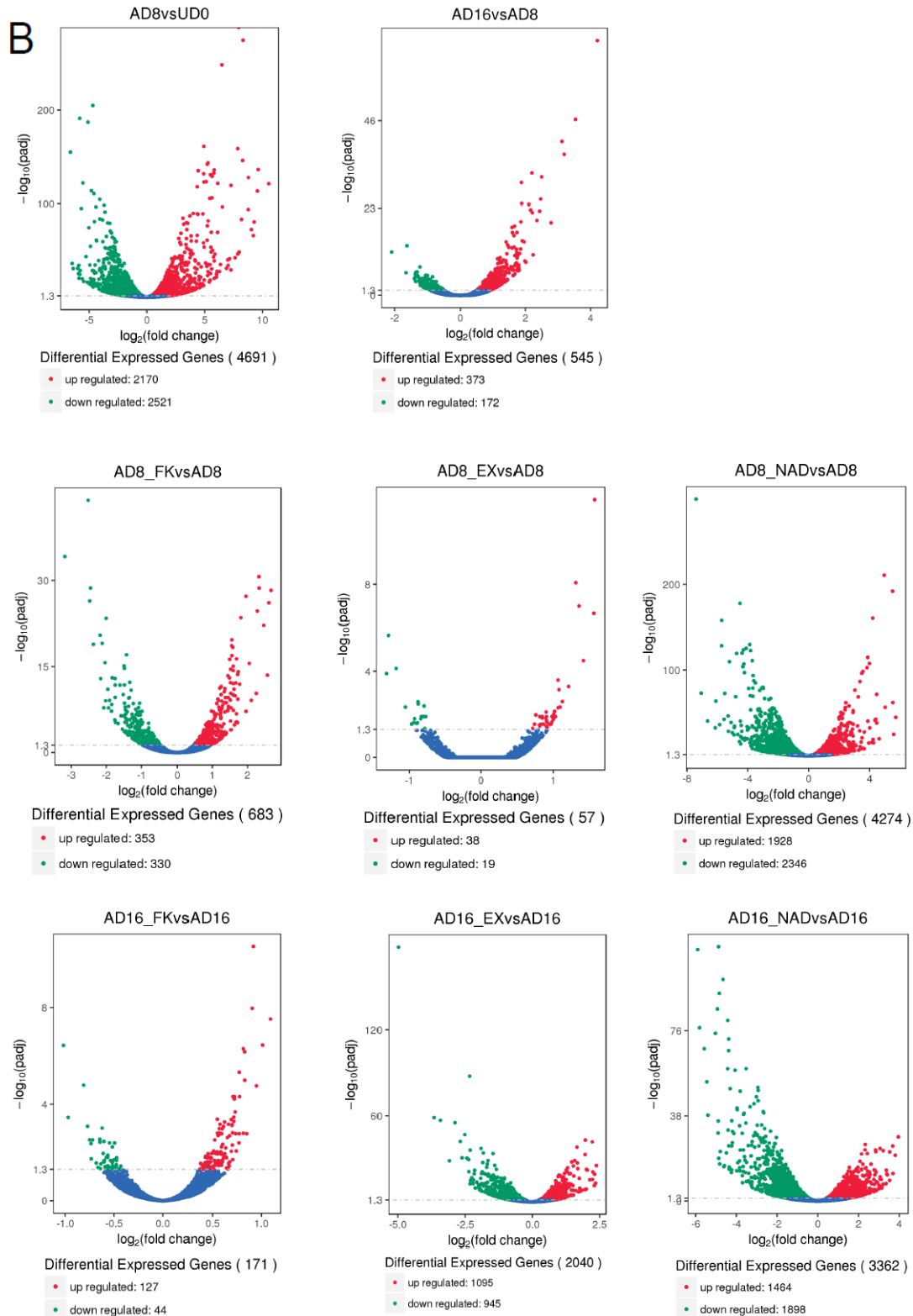


**Fig. S2. RNA-seq data analyses.** **A)** Principal component analyses (PCA) was computed and plotted in two dimensional PCA score plots, showing clustering of undifferentiated hMSC (UD) vs differentiated cells (top), NAD<sup>+</sup>-treated (AD8\_NAD, AD16\_NAD) vs untreated cells (middle) and day 8 (adipocyte commitment) vs day 16 (terminally differentiated adipocytes) (bottom). **B)** Volcano plots show DE genes from the indicated comparisons (FDR-adjusted P-value <0.05).

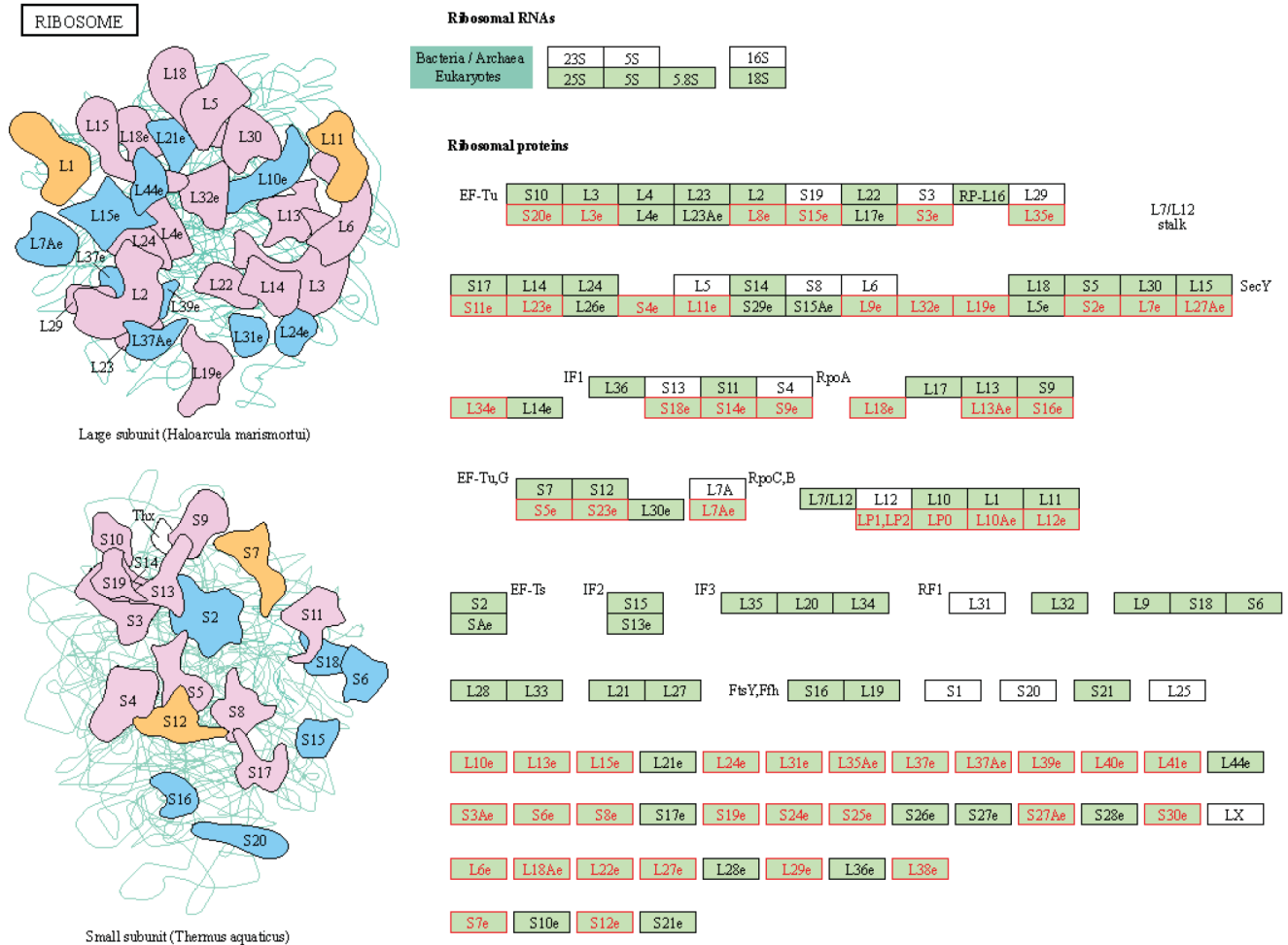


**Fig. S3. Expression of the ribosomal pathway is impaired by excess of NAD<sup>+</sup> during adipogenesis.** Illustration of the Ribosomal Pathway according to the KEGG. Ribosomal components are illustrated (left) and listed (right). Ribosomal proteins whose mRNA expression is consistently downregulated by NAD<sup>+</sup> treatment during adipogenesis are highlighted in red color..

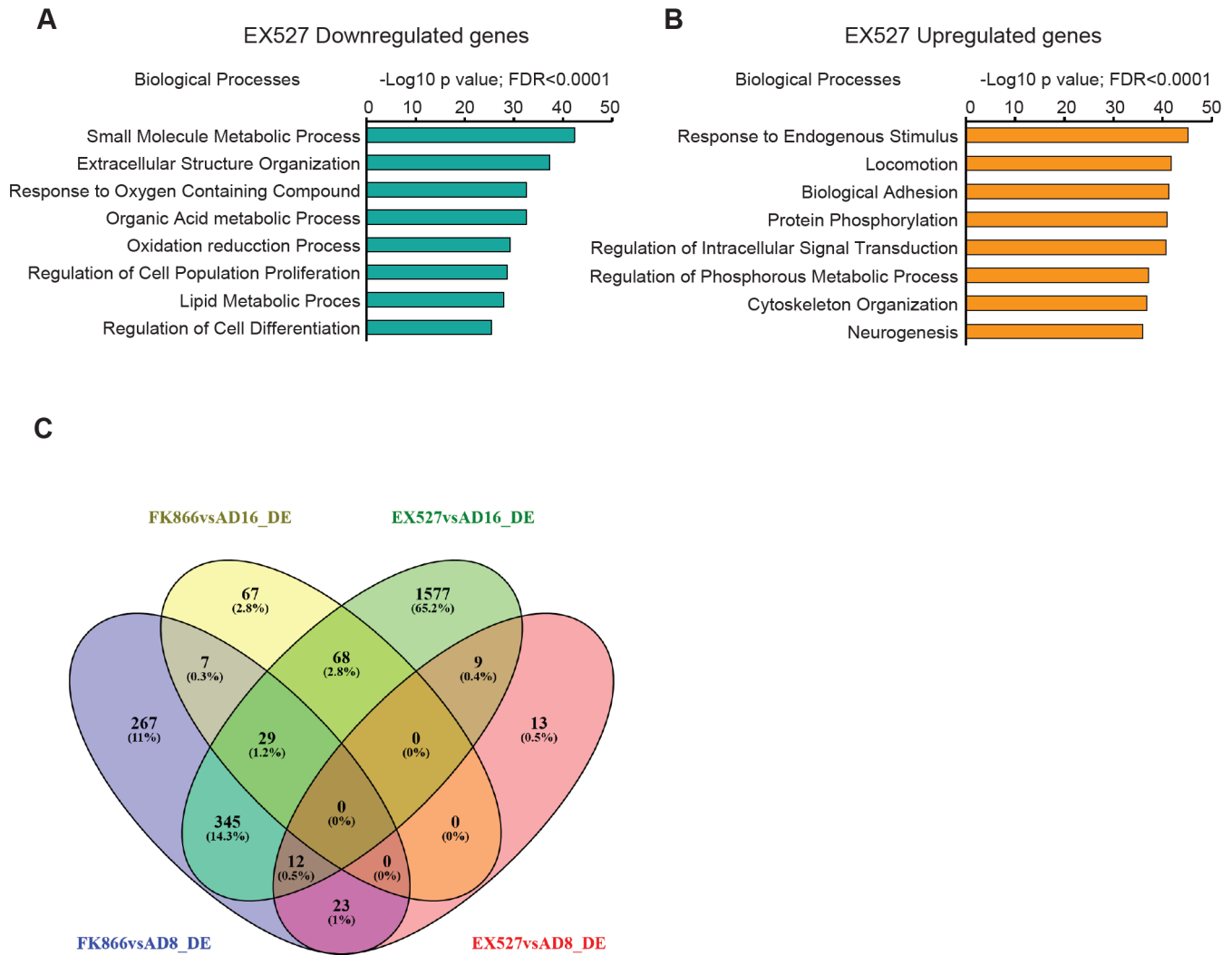


**Fig. S4. Transcriptional rewiring during adipogenic differentiation triggered by SIRT1 or NAPT inhibition.** **A, B)** Biological processes enrichment analyses from genes downregulated (**A**) or upregulated (**B**) by EX527 treatment during adipogenic differentiation, at day 16 after induction, compared with untreated, terminally differentiated adipocytes. **C)** Venn diagram shows overlapping DE genes between indicated comparisons: FK866vsAD8\_DE and FK866vsAD16\_DE: mRNA was analyzed from cells during adipogenic differentiation (day 8 or day 16) from untreated (AD) or treated with 1nm FK866 during differentiation. EX527vsAD8\_DE and EX527vsAD16\_DE: mRNA was analyzed from cells during adipogenic differentiation (day 8 or day 16) from untreated (AD) or treated with 50 $\mu$ M EX527 during differentiation.

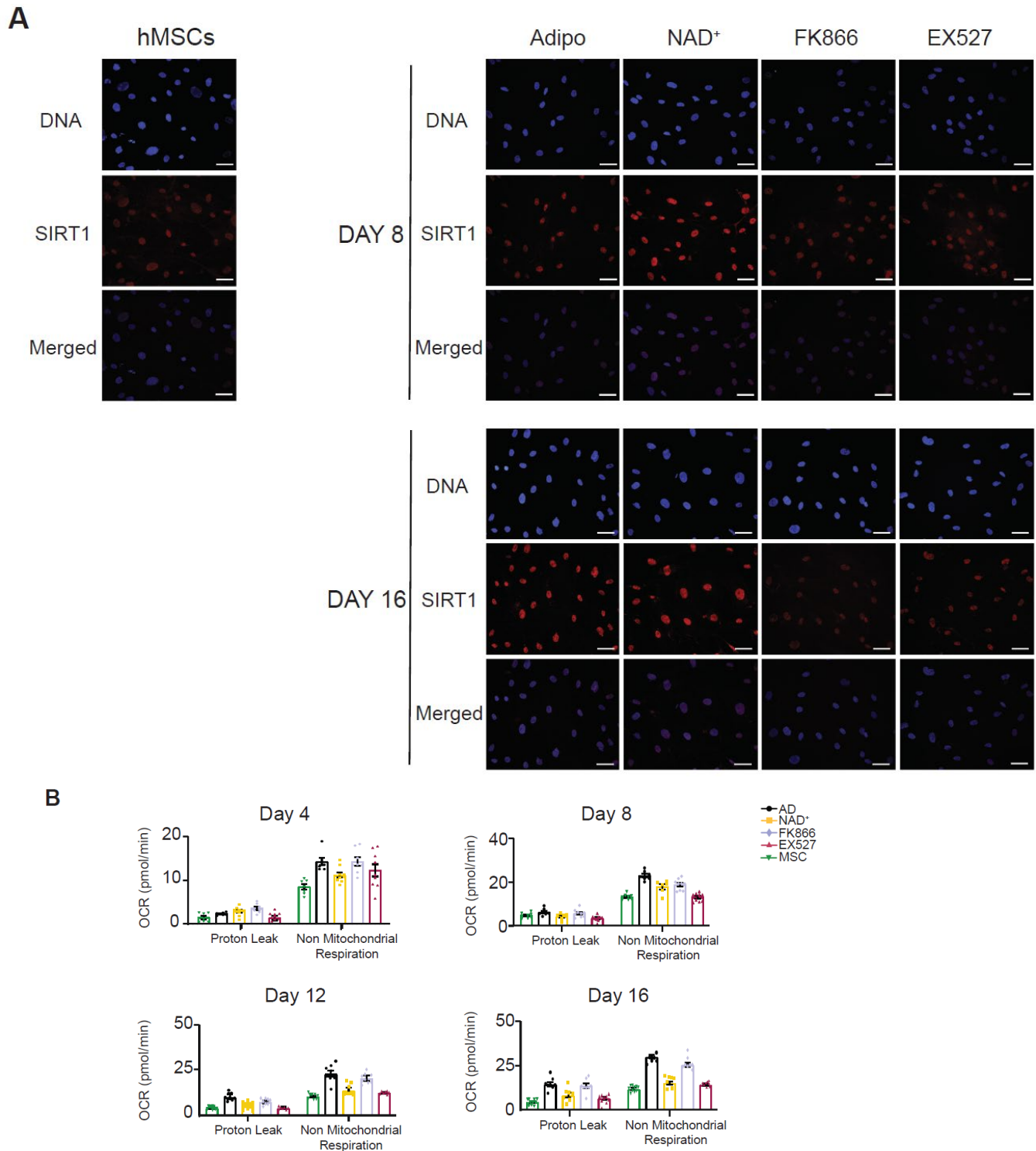


**Fig. S5. SIRT1 levels and mitochondrial bioenergetics during adipogenic differentiation. A)** SIRT1 protein levels and subcellular localization were analyzed by immunofluorescence at days 8 and 16 after adipogenic induction on hMSC. Cells were either untreated (Adipo), or treated with the indicated compounds. n= 2 biological and 7 technical replicates. **B)** Mitochondrial bioenergetic parameters calculated from extracellular flux analyses: Proton leak and non-mitochondrial respiration. AD: adipogenic induced cells; NAD<sup>+</sup> adipogenic induced cells treated with 5 mM NAD<sup>+</sup>; FK866: adipogenic induced cells treated with 1 nM FK866; EX527: adipogenic induced cells treated with 50  $\mu$ M EX527. MSC: untreated, undifferentiated hMSC.

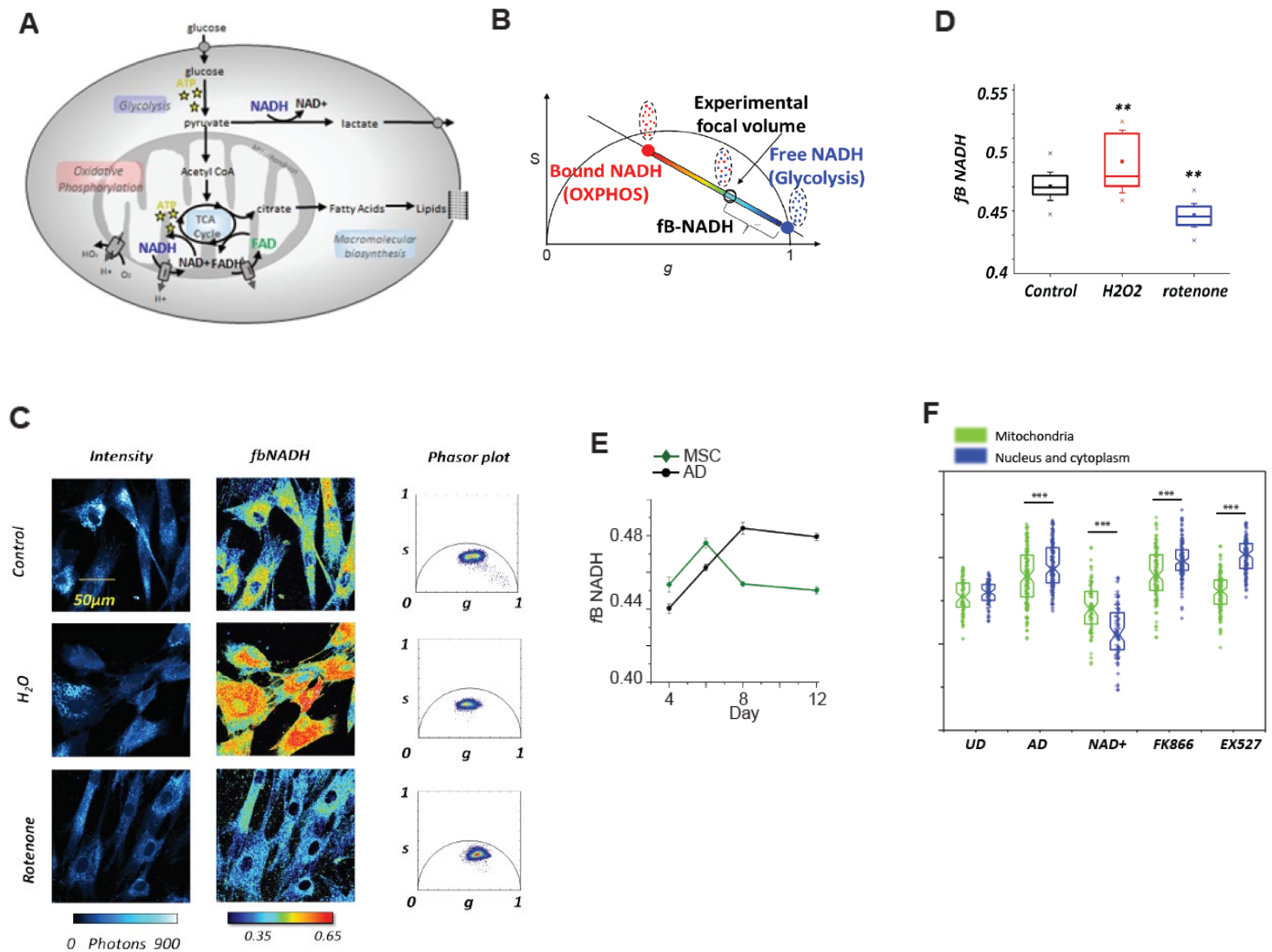


**Fig. S6. Metabolic trajectories assessed by 2P-FLIM on NADH. A)** Schematic representation of cellular metabolism. Glucose breakdown through glycolysis and the TCA cycle generates reduced NADH and FADH<sub>2</sub>. Quiescent cells have a basal rate of glycolysis, converting glucose to pyruvate, which is then oxidized in the TCA cycle. As a result, the majority of ATP is generated by oxidative phosphorylation (OXPHOS). Non proliferating, differentiated cells are characterized by a low NADH/NAD<sup>+</sup> ratio. During proliferation, the large increase in glycolytic flux rapidly generates ATP in the cytoplasm. Most of the resulting pyruvate is converted into lactate by lactate dehydrogenase A, which regenerates NAD<sup>+</sup> from NADH. Proliferating cells are characterized by a high NADH/NAD<sup>+</sup> ratio. Rotenone blocks the respiratory chain via complex I while H<sub>2</sub>O<sub>2</sub> increase the NAD<sup>+</sup>:NADH ratio. **B)** Metabolic trajectory between free NADH and bound NADH indicates a shift from a glycolytic to a OXPHOS cellular phenotype as free/bound NADH ratio corresponds to NAD<sup>+</sup>:NADH ratio. The fraction of bound NADH (fb\_NADH) of the experimental point is graphically calculated from the location of free NADH. **C)** Representative images of intensity, fb\_NADH and phasor plot of hMSCs with different treatments: control, rotenone (respiratory chain inhibitor) and H<sub>2</sub>O<sub>2</sub> (induces oxidative stress). Accumulation of reduced NADH by blocking the respiration chain shifts the cellular metabolic signature toward free NADH, while oxidative stress shifts the cellular metabolic signature towards bound NADH. **D)** Quantification of fraction of bound NADH in a ROI with different metabolic treatments. One-way ANOVA followed by Tukey's post test. \* p < 0.05, \*\* p < 0.01. **E)** Quantification of fraction of bound NADH during adipogenic differentiation at with (black) or without adipogenic culture medium (dark green). Data is presented as mean ± SEM **F)** Quantification of fb\_NADH in mitochondria (green) and in nucleus/cytoplasm (blue) in single cells at day 8 of adipogenic differentiation in the absence (AD) or in the presence of the indicated treatments. hMSC (UD) were also assessed. n = 63-125 cells; \*\*\*p < 0,001, Student's t-test.

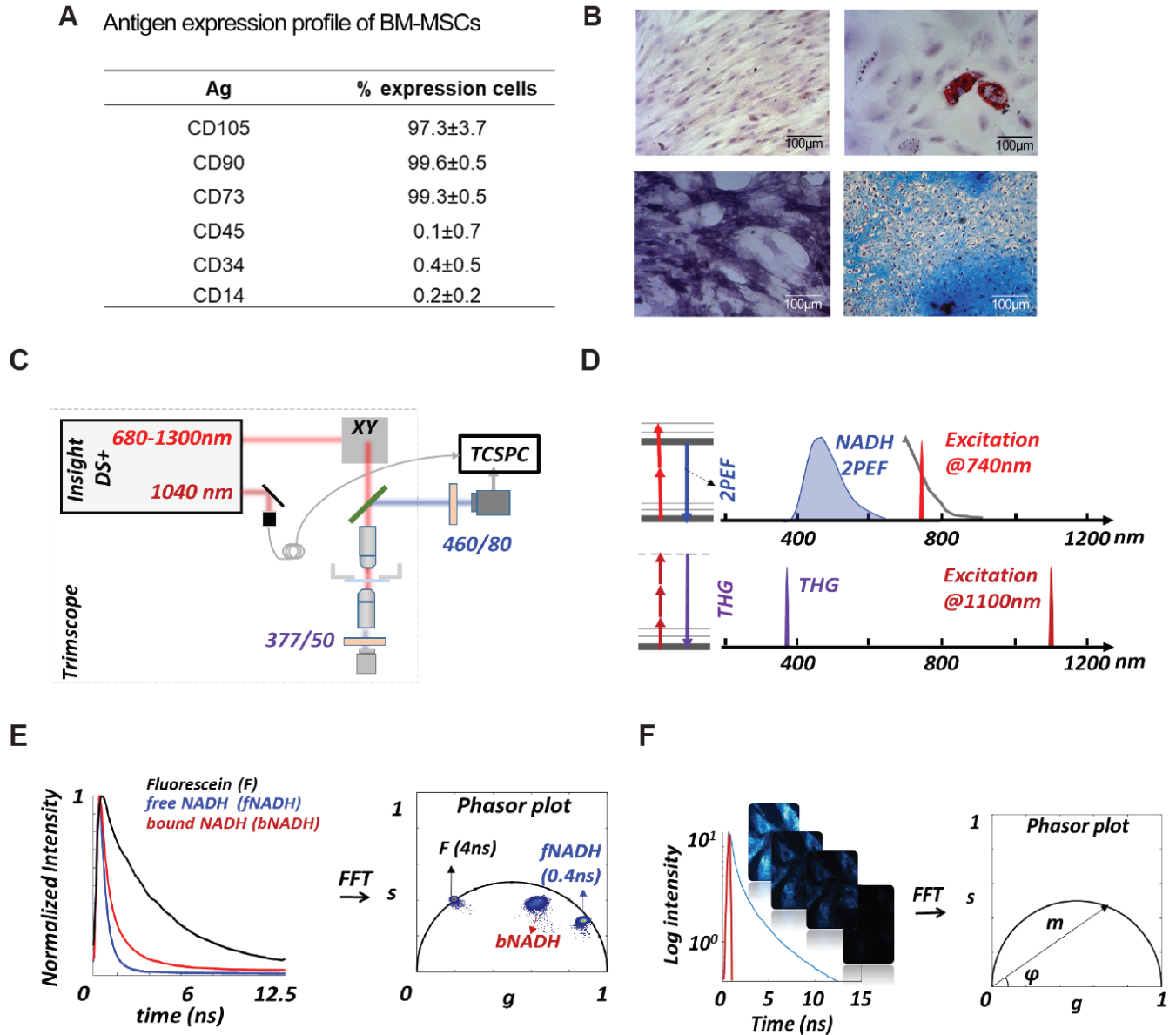


**Fig. S6. hMSC characterization and experimental setup.** **A)** Expression cell markers in MSCs was determined by Flow Cytometry, data correspond to mean percentage of cells positive to each marker  $\pm$  SD,  $n=3$  biological replicates. **B)** hMSCs stained with toluidine blue (top left), adipogenic differentiation was determined by the presence of lipid vacuoles positive to ORO (top right), osteogenic differentiation was determined by Alkaline Phosphatase assay (bottom left) and chondrogenic differentiation was assessed by matrix positive to Alcian blue in cryosections of micromasses (bottom right).  $n=3$  biological replicates. **C)** Scheme of the experimental setup used for this work. **D)** Principles of 2 photon excitation fluorescence and THG signal generation: Two-photon excitation of NADH occurs at 740 nm with emission collected with band-pass filters centered at 460nm, which resulted primarily from NADH. The excitation of THG occurred at 1100nm, with emission collected with a band-pass filter centered at 377nm. **E)** Example of fluorescence intensity decay of fluorescein and free and bound NADH in solution and their locations in the phasor plot. **F)** The multi-exponential fluorescence intensity decay in every pixel of the image is transformed with a Fourier transform; the real ( $g$ ) and imaginary ( $s$ ) parts are plotted in the graphical phasor plot.



**Dataset S1 (separate file). Summary of mapping results.** Sample name: sample identification; Total reads: total clean reads suitable for analysis; Total mapped: numbers of reads being mapped on the genome; Uniquely mapped reads: numbers of reads being mapped to a single position of the genome; Multiple mapped reads: numbers of reads being mapped to more than one genomic sites; Total mapping rate:  $(\text{mapped reads})/(\text{total reads}) * 100$ ; Uniquely mapping rate:  $(\text{uniquely mapped reads})/(\text{total reads}) * 100$ ; Multiple mapping rate:  $(\text{multiple mapped reads})/(\text{total reads}) * 100$ .

**Dataset S2 (separate file).** List of differentially expressed genes from NAD<sup>+</sup>-treated cells genes and their functional analyses.

**Dataset S3 (separate file):** List of DE genes in from EX527-treated cells at terminal differentiation (day 16) and their functional analyses.

**Dataset S4 (separate file):** List of DE genes in from FK866-treated cells at terminal differentiation (day 16) and their functional analyses